Satellite observations reveal a decreasing albedo trend of global urban cities over the past 35 years

Satellite observations reveal a decreasing albedo trend of global urban cities over the past 35 years

Shengbiao Wu[1], Xingwen Lin[2], Zunjian Bian[3], Mathew Lipson[4], Raffaele Lafortezza[5,6], Qiang Liu[7], Sue Grimmond[8], Erik Velasco[9], Andreas Christen[10], Valéry Masson[11], Ben Crawford[12], Helen Claire Ward[13], Nektarios Chrysoulakis[14], Krzysztof Fortuniak[15], Eberhard Parlow[16], Wlodzimierz Pawlak[15], Nigel Tapper[17], Jinkyu Hong[18], Je-Woo Hong[19], Matthias Roth[20], Jiafu An[21], Chen Lin[22], Bin Chen[1,23-24,*]

(1) Landscape Architecture, Faculty of Architecture, The University of Hong Kong, Pokfulam, China (shengwu@hku.hk)
(2) College of Geography and Environmental Sciences, Zhejiang Normal University, Jinhua 321004, China (linxw@zjnu.edu.cn)
(3) Stake Key Laboratory of Remote Sensing Science, Aerospace Information Research Institute, CAS, Beijing 100083, China (bianzj@aircas.ac.cn)
(4) Australian Research Council (ARC) Centre of Excellence for Climate System Science, Climate Change Research Centre, Level 4, Mathews Building, UNSW Sydney, New South Wales, 2052, Australia (m.lipson@unsw.edu.au)
(5) Department of Soil, Plant and Food Sciences (Di.S.S.P.A.), University of Bari Aldo Moro, Via Amendola 165/A 70126 Bari, Italy (raffaele.lafortezza@uniba.it)
(6) Beijing Forestry University, Beijing 100083, China (raffaele.lafortezza@uniba.it)
(7) Pengcheng Laboratory, Shenzhen 518055, China (liuq03@pcl.ac.cn)
(8) Department of Meteorology, University of Reading, Reading, RG6 6ET, United Kingdom (c.s.grimmond@reading.ac.uk)
(9) Molina Center for Energy and the Environment, Boston, USA (evelasco@mce2.org)
(10) Environmental Meteorology, Institute of Earth & Environmental Sciences, Faculty of Environment and Natural Resources, University of Freiburg, Freiburg, Germany (andreas.christen@meteo.uni-freiburg.de)
(11) CNRM, University of Toulouse, Météo-France and CNRS, Toulouse, France (valery.masson@meteo.fr)
(12) Geography and Environmental Sciences, University of Colorado, Denver, Colorado, USA (benjamin.crawford@ucdenver.edu)
(13) Department of Atmospheric and Cryospheric Sciences, University of Innsbruck, Innsbruck, Austria (Helen.Ward@uibk.ac.at)
(14) FORTH, Institute of Applied and Computational Mathematics, Remote Sensing Lab, Heraklion, Greece (zedd2@iacm.forth.gr)
(15) Dept Meteorology & Climatology, University of Lodz, Lodz, Poland krzysztof.fortuniak@geo.uni.lodz.pl; wlodzimierz.pawlak@geo.uni.lodz.pl
(16) Department for Environmental Sciences, Meteorology, Climatology and Remote Sensing, University Basel, CH-4056 Basel, Switzerland (eberhard.parlow@unibas.ch)
(17) School of Earth, Atmosphere and Environment, Monash University, Melbourne, Australia (nigel.tapper@monash.edu)
(18) Ecosystem-Atmosphere Process Lab, Department of Atmospheric Sciences, Yonsei University, Seoul, Republic of Korea (jhong@yonsei.ac.kr)
(19) Korea Environment Institute, Sejong, Republic of Korea (jwhong@kei.re.kr)
(20) Department of Geography, National University of Singapore, Singapore, Singapore (geomr@nus.edu.sg)
(21) Department of Finance and Insurance, Faculty of Business, Lingnan University, Hong Kong SAR, China (jiafuan@ln.edu.hk)
(22) Faculty of Business and Economics, The University of Hong Kong, Hong Kong SAR, China (chenlin1@hku.hk)
(23) Urban Systems Institute, The University of Hong Kong, Hong Kong SAR, China (binley.chen@hku.hk)
(24) HKU Musketeers Foundation Institute of Data Science, The University of Hong Kong, Hong Kong SAR, China (binley.chen@hku.hk)
* Corresponding Author: Bin Chen (binley.chen@hku.hk)

Abstract

Urban surface albedo is an essential biophysical variable in the surface energy balance across all scales, from micro-scale (materials) to global scale, changing with land cover and three-dimensional (3-D) structure over urban areas. Urban albedos are dynamics over space and time but have not yet been quantified over global scales due to the lack of high-resolution albedo datasets. Here, we combined the direct estimation approach and Landsat surface reflectance product to generate a 30-m-resolution annual surface albedo dataset for 3037 major cities (area > 50 km^2) worldwide for the period from 1986 to 2020, allowing spatial patterns and long-term temporal trends to be explored with possible causal drivers, and quantification of the surface radiative forcing from these albedo changes. Evaluation of this new albedo dataset using global urban flux tower-based measurements demonstrates its high accuracy with an overall bias and root-mean-square-error (RMSE) of 0.005 and 0.025, respectively. Analysis of the dataset reveals an overall trend of decreasing albedo for the 35-year evaluation period (1986-2020), which is robust accounting for a series of uncertainties from training sample representativeness, Landsat data uncertainty, seasonal variation, and snow-cover confounding impacts. Our results reveal that urban greening (measured by the Normalized Difference Vegetation Index (NDVI) trend) can well explain the total variances in the albedo trend for the 35-year period through two different pathways of tree planting and urban warming-enhanced vegetation growth. The decrease in urban albedo caused a warming effect indicated by positive surface radiative forcing, with a global city-level average surface radiative forcing of 2.76 $W \cdot m^{-2}$. These findings enhance our understanding of urbanization's impacts on albedo-related biophysical processes and can provide information to quantify urban surface radiation energy and design effective mitigation strategies to reduce urban warming (e.g., urban heat islands).

Keywords: Biophysical process; NDVI; Radiative forcing; Landsat; MODIS; Surface albedo

1. Introduction

Urban areas represent the principal land cover that is most affected by intensive anthropogenic activities from replacing agricultural, forested or natural landscapes with impervious surfaces (Seto et al. 2012). Urbanization modifies the carbon exchange between the surface and atmosphere (e.g., anthropogenic emissions of carbon dioxide (CO_2) from domestic heating, transport, industry and services, and electricity generation; Ribeiro et al. 2019; Wang et al. 2015), as well as changes surface radiative properties and energy partitioning (e.g., albedo and evapotranspiration; Cao et al. 2016; Schwaab et al. 2021), and thus modifies biophysical variables (e.g., air temperature). This can result in nocturnal canopy air temperatures being warmer in urban areas than the surrounding non-urban areas, known as the canopy layer urban heat island (CL-UHI) (Estoque et al. 2020; Oke, 1982). With a global urban population of 4.2 billion (around 55% of the total population in 2018) projected to increase to 9.7 billion (about 68% of the total population) by 2050 (UNDESA, 2019), the well-being of urban residents is at critical risk and simultaneously impact by urban-climate phenomena, such as the CL-UHI (Huang et al. 2020; Hsu et al. 2021). Improving our understanding of biophysical processes in cities can help to create more livable environments.

Surface albedo change can directly alter the biophysical processes of surface energy balance from micro (materials) to local and to global scales. Urbanization causes albedo changes by modifying surface materials and three-dimensional (3-D) structures (Shen et al. 2021). For example, anthropogenic land cover changes between 1700 and 2005 are estimated to have caused a 0.00106 increase in global mean albedo, that is linked to a negative radiative forcing of -0.15 ± 0.10 $W \cdot m^{-2}$ (Ghimire et al. 2014; Myhre et al. 2014). For a long time, the use of highly reflective urban materials (e.g., white rooftops and light-colored pavements) has been actively encouraged as method to mitigate the surface-UHI (S-UHI) effect and improve human comfort (Morini et al. 2016; Rosso et al. 2018). Numerous regional and global climate simulations have shown albedo-related impacts. A 0.1 increase in albedo in urban areas (e.g., rooftops and pavements) has been estimated to be able to reduce the global average surface temperature by 0.01-0.07 K, which is equivalent to a 25-150 billion ton offset in CO_2 emissions (Akbari et al. 2012; Menon et al. 2010; Xu et al. 2020).

Urbanization impacts on surface albedo are multifaceted. Initial urbanization, changing a natural vegetated surface (e.g., forest and grassland) to light colored short building may increase surface albedo (Kuang et al. 2019), but the same materials with denser 3-D urban morphology will generate more shadows, reducing the bulk surface albedo (Christen and Vogt, 2004; Groleau and Mestayer, 2013). The net surface albedo change depends on both urban cover materials and building arrangements (Falasca et al. 2019; Qin, 2015; Santamouris and Fiorito, 2021; Yang and Li, 2015). Satellite remote sensing can quantify these net effects with global coverage. Coarse-resolution satellites in previous studies based on the 500-m-resolution Moderate-Resolution Imaging Spectroradiometer (MODIS) and Global LAnd Surface Satellite (GLASS) albedo products were not able to accurately detect the fine-scale heterogeneity of urban albedo (Chrysoulakis et al. 2018; Hu et al. 2016; Tang et al. 2018). Use of higher-resolution satellite observations (e.g., 30-m Landsat and 10-m Sentinel-2) demonstrated their potential to monitor fine-scale urban albedo (Bonafoni and Sekertekin, 2020; Guo et al. 2022; Trlica et al. 2017).

However, our spatiotemporal knowledge of urban albedo is limited for several reasons. First, existing satellite-based albedo studies are restricted to very few (≤ 11) cities (Guo et al. 2022; Trlica et al. 2017), so the spatiotemporal trends may be city-specific. Second, the underlying drivers controlling the spatiotemporal patterns of surface albedo and their resulting climatic effects remain largely unclear. Urbanization are complex physical, socioeconomic, and cultural processes in 3-D space, involving extent expansion of new impervious areas (Liu et al. 2020; Zhang and Seto, 2011) and increase in human modification on mature urban areas, such as building construction and greening activity (Theobald et al. 2020; Zhou et al. 2022). Previous studies attributed urban albedo variations to land cover change from natural lands to new urban structure by making the use of two-baseline-year datasets, without accounting for human modification activities (Ouyang et al. 2022). For example, large-scale tree planting in cities is a global agreement and effort to mitigate urban heat stress from climate warming and CL-UHI effects (Schwaab et al. 2021). Around 70% of cities worldwide witness urban greening phenomenon with increasing vegetation coverage (Sun et al. 2020; Zhang et al. 2021) and enhanced vegetation growth due to CO_2 fertilization and longer growing seasons (Hwang et al. 2022; Meng et al. 2020; Wang et al. 2019). These actions have substantially reshaped urban landscapes, but to what extent urban greening impacts the change of surface albedo and albedo-related climatic effects remains unknown.

In such a context, the main objective of this study is to explore the spatiotemporal characteristics of albedo in cities globally and to decipher the underlying drivers of albedo change. By applying our previously developed direct estimation approach on the Google Earth Engine (GEE) cloud-computing platform, we construct an annual mean albedo dataset covering 35 years (1986-2020) for 3037 major global cities. Based on the novel dataset, we analyze the spatial and temporal patterns of urban albedo and assess the causes of albedo change linked to vegetation greening observed in Landsat-derived normalized difference vegetation index (NDVI) data. Lastly, we quantify the albedo-induced surface radiative forcing to model climatic responses from urban surface albedo change.

2. Study area and materials

2.1. City areas

The city areas were extracted from the 2018 Global Urban Boundary (GUB) product, which is based on 30-m-resolution global artificial impervious area product (GAIA; Li et al. 2020), using two criteria (Chen et al. 2022): (1) a spatial extent larger than 50 km^2; and (2) availability of at least 30-year valid Landsat observations during the 35 evaluated years (1986-2020). A total of 3037 urban areas globally (hereafter referred to as cities) satisfied these criteria and were selected (**Fig. 1**). Almost all cities have over 20 available Landsat images for each one-year cycle, with the annual average observation number ranging from 21 to 40 and a mean value of 30, indicating the capability to capture inter- and intra-year variations of urban surface albedo (**Figs. S1** and **S2**).

2.2. Datasets

Five multi-source datasets are used in this study for different purposes: (1) surface reflectance data (i.e., Landsat-5, Landsat-7, and Landsat-8 surface reflectance products; Gorelick et al. 2017); (2) surface Bidirectional Reflectance Distribution Function (BRDF) data (i.e., MCD43A1; Wang et al. 2018); (3) surface albedo data, (i.e., flux tower-based measurements and MCD43A3; Feigenwinter et al. 2018; Lipson et al. 2022a, 2022b; Wang et al. 2018); (4) land cover type data (i.e., European Space Agency (ESA) WorldCover and MCD12Q1; Sulla-Menashe et al. 2018; Zanaga et al. 2021); and (5) downward solar radiation data, (i.e., the Bias-adjusted RAdiation Dataset (BaRAD) product; Chakraborty and Lee, 2021). **Table 1** summarizes the ancillary information of these datasets, including data category, dataset name, spatial coverage, ground resolution, observation period, usage description, and related references**. Table 2** provides detailed information for the 21 urban flux towers used for albedo validation.

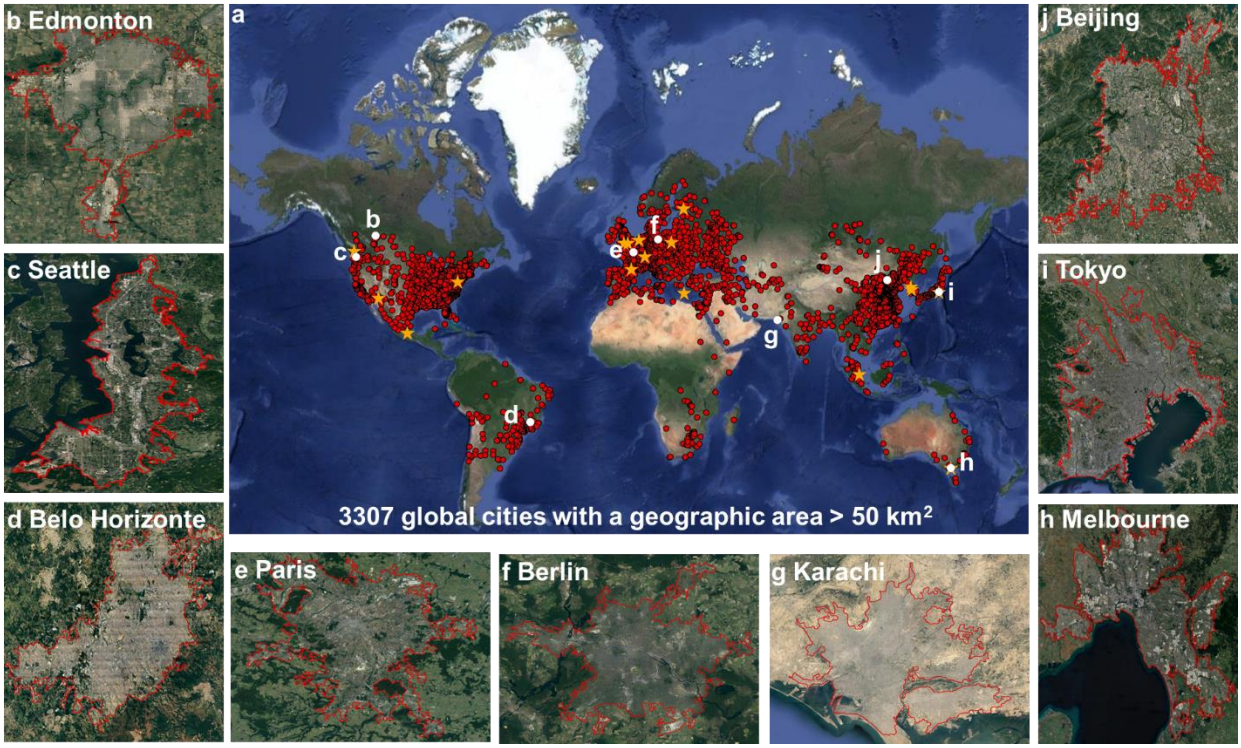

Fig. 1. Urban areas (cities) used in this study. (a) City location globally (red dots), urban flux towers (yellow pentagrams), and example of nine cities with boundaries (red polygons) as defined by the Global Urban Boundary (GUB) product in 2018: (b) Edmonton, (c) Seattle, (d) Belo Horizonte, (e) Paris, (f) Berlin, (g) Karachi, (h) Melbourne, (i) Tokyo, and (j) Beijing. The 3037 global cities are selected with an area extent larger than 50 km2. 21 worldwide urban flux tower sites come from two collaborative projects: 19 flux sites from the Urban-PLUMBER multi-site model evaluation project (Lipson et al. 2022a, 2022b) and 2 flux sites from the URBANFLUXES project (Chrysoulakis et al. 2018; Feigenwinter et al. 2018). Background and city pictures are extracted from the Basemap of Google Earth (Google. Inc).

2.2.1. Landsat surface reflectance product

We used 35-years (1986-2020) of the Landsat Level-2 surface reflectance (Collection 2, Tier 1) product with a 30-m spatial resolution derived from three Landsat satellites (i.e., Landsat-5 TM, Landsat-7 ETM+, and Landsat-8 OLI; Gorelick et al. 2017, **Table 1**). Landsat provides the longest high-quality global surface reflectance record available (Wulder et al. 2022). Landsat-5 TM and Landsat-7 ETM+ sensors have six spectral bands spanning three visible (i.e., blue, green, and red), one near-infrared (NIR), and two shortwave infrared (SWIR) bands, whereas Landsat-8 OLI has one additional ultra-blue spectral band. The pixel-level quality assurance (QA) auxiliary data for each surface reflectance dataset gives a bitmask metric indicating cloud, cloud shadow, snow, and ice conditions. To minimize the uncertainty caused by the Landsat-7 scan line off failure on albedo estimation (Qiu et al. 2021; Zhang and Roy, 2016), we primarily focused on the use of Landsat-5 and Landsat-8 satellite data, with data availabilities of 26-year (1986-2011) Landsat-5 TM, 2-year (2012-2013) Landsat-7 ETM+, and 7-year (2014-2020) Landsat-8 OLI.

2.2.2. MODIS BRDF/albedo product

We used the 500-m spatial resolution MODIS BRDF product (MCD43A1, Collection 6; **Table 1**) in 2000-2020 to provide a high-quality surface BRDF/albedo training library (Wang et al. 2018). MCD41A1 is the most accurate satellite BRDF/albedo product and has been widely used for the training and calibration of the direct estimation approaches (Guo et al. 2022; Qu et al. 2013). In addition, the MCD43A3 albedo product was used for the spatiotemporal analysis of urban surface albedo for comparisons with Landsat albedo. MCD43A3 is derived from MCD43A1 and provides black-sky albedo (BSA) and white-sky albedo (WSA) data at local solar noon for MODIS seven spectral bands and three broadbands (i.e., visible, NIR, and shortwave).

2.2.3. Land cover type products

Two land cover type products are used (**Table 1**): 10-m ESA WorldCover for 2020, and 500-m MCD12Q1 products (Collection 6) from 2001 to 2020, for selecting training samples. WorldCover is generated from Sentinel-1 and Sentinel-2 data, with a similar algorithm framework for the annual Copernicus Global Land Service Land Cover (CGLS-LC) product (Buchhorn et al., 2020). This dataset provides 11 land cover classes (i.e., tree cover, shrubland, grassland, cropland, built-up, bare/sparse vegetation, snow and ice, open water, herbaceous wetland, mangroves, and moss and lichen) with an overall global accuracy of 74.4% (Zanaga et al. 2020). It is freely accessible to the academic community (Zanaga et al. 2020). MCD12Q1 is generated by a supervised classification approach from MODIS reflectance with five legacy classification schemes (Sulla-Menashe and Friedl, 2018). We selected the International Geosphere-Biosphere Programme (IGBP) classification scheme for data analysis. The "built-up" definitions in these two land cover products have a slight difference. For WorldCover, "built-up" is defined as land covered by buildings, roads and other man-made structures, which excludes urban green areas (Zanaga et al. 2020). For MCD12Q1, "urban and built-up lands" is defined as surface covered by at least 30% of impervious area, such as building materials, asphalt, and vehicles (Sulla-Menashe and Friedl, 2018).

2.2.4. Surface downward solar radiation data

We used the 40-year (1980-2019) 0.5° × 0.625° monthly BaRAD solar radiation dataset (**Table 1**) owing to its temporal window overlapping with Landsat. BaRAD is generated from the Modern-Era Retrospective analysis for Research and Applications, version 2 (MERRA-2) global reanalysis dataset using a bias-correction random forest algorithm, trained with Global Energy Balance Archive (GEBA) observations from 2500 worldwide ground stations (Wild et al. 2017). BaRAD is bias-adjusted (cf. MERRA-2) thus has high accuracy (Chakraborty and Lee, 2021). BaRAD provides three radiation components: total incoming shortwave, incoming direct beam, and incoming diffuse radiation. BaRAD data are used here to determine: (1) the fraction of diffuse radiation relative to the total incoming shortwave radiation, for the blue-sky albedo calculation (**Section 3.1**); and (2) the surface radiative forcing induced by albedo changes (**Section 3.5**).

2.2.5. Tower-based radiation flux measurements

To evaluate the accuracy of our algorithm, we used downward and upward solar radiation measurements from 21 urban flux towers located throughout the world, including cities in Asia, Australia, Europe, and North America (Fig. 1a). The data collected by these towers were put together as part of two collaborative projects: Urban-PLUMBER (19 sites; Lipson et al. 2022a, 2022b) and URBANFLUXES (2 sites; Chrysoulakis et al. 2018; Feigenwinter et al. 2018). The sensors on these towers are mounted at heights ranging from 2 to 60 meters above the ground, with viewing footprints where impervious surfaces (i.e., buildings, roads, paved areas) cover between 31% and 97% of the plan area (Fig. 2; Table 2). The radiation flux measurements are used as ground truths for assessing the accuracy of surface albedo estimates derived from Landsat satellites.

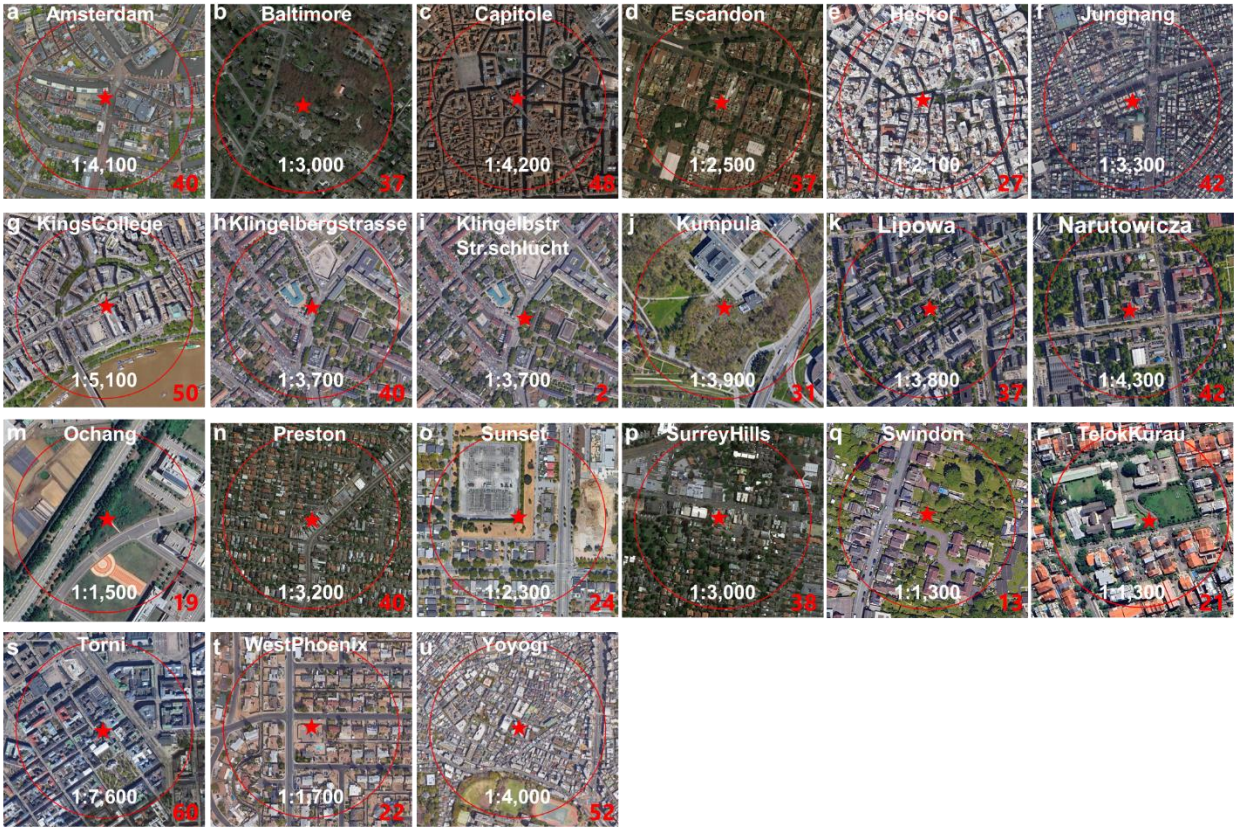

Fig. 2*. Google Earth satellite images of flux sites (red pentagrams) and the associated radiation footprint areas (red circles) for* ***(a)*** *Amsterdam,* ***(b)*** *Baltimore,* ***(c)*** *Capitole,* ***(d)*** *Escandon,* ***(e)*** *Heckor,* ***(f)*** *Jungnang,* ***(g)*** *KingsCollege,* ***(h)*** *Klingelbergstrasse,* ***(i)*** *KlingelbstrStr.schlucht,* ***(j)*** *Kumpula,* ***(k)*** *Lipowa,* ***(l)*** *Narutowicza,* ***(m)*** *Ochang,* ***(n)*** *Preston,* ***(o)*** *Sunset,* ***(p)*** *SurreyHills,* ***(q)*** *Swindon,* ***(r)*** *TelokKurau,* ***(s)*** *Torni,* ***(t)*** *WestPhoenix, and* ***(u)*** *Yoyogi. The map scales and tower heights (in meters) are shown at the bottom of each image in white and red, respectively. Note: Footprint area (with a 25-m diameter) of the KlingelbstrStr.schlucht site in panel* ***(i)*** *is overlapped by red pentagram symbol.*

3. Methods

3.1. Estimation of annual urban surface albedo from Landsat

We adopted our recently developed direct estimation approach to retrieve surface albedo from Landsat satellites (Lin et al. 2022), with three key steps summarized as follows (Fig. 3):

(1) *Selection of high-quality surface BRDF/albedo datasets.* High-quality BRDF/albedo training datasets are the key to the direct estimation approach. To this end, we used the MCD43A1 BRDF/albedo product with ESA WorldCover and MCD12Q1 land covers to screen the BRDF/albedo library that is representative at 30-m scale (Lin et al. 2022) with four criteria: (i) high assurance with the pixel-level QA of 0; (ii) homogeneous coverage (with the pixel-level land cover purity ≥ 95% indicated by the 10-m ESA WorldCover data); (iii) diverse land cover (including 16 dominant land types following the IGBP classification scheme); and (iv) reasonable data range (that refers to the pairs of reflectance and albedo within a physical range of 0-1). We considered this surface BRDF/albedo dataset from mixed land covers as a general scheme and compared it with the BRDF/albedo dataset from pure urban land cover

(referred to as urban scheme) in the sensitivity analysis of algorithm development (Section 5.1.1), which shows a consistent performance.

(2) *Generation of training and testing datasets*. Based on the selected BRDF/albedo library, we simulated Landsat-like surface reflectance in two steps. First, we simulated MODIS-like surface reflectance across its seven spectral bands using the linear RossThick-LiSparseR BRDF model (Lucht et al. 2000) with optimized angular settings (i.e., a 2° interval for solar zenith, viewing zenith, and local solar zenith angles; and a 5° interval for relative azimuth angle). Second, we converted the MODIS-like surface reflectance to the Landsat-like surface reflectance using band conversion coefficients derived using similar approaches to Qu et al. (2013). Considering the different spectral configurations for Landsat satellites (Table S1), we simulated surface reflectance datasets across six spectral bands for Landsat-5 TM and Landsat-7 ETM+, and across seven spectral bands for Landsat-8 OLI. We also simulated surface shortwave albedo from the MODIS BRDF/albedo library in two steps. First, we simulated spectral BSA and WSA datasets under clear-sky and perfectly diffuse illumination conditions, respectively. Second, we converted the spectral BSA and WSA albedo datasets to shortwave albedo using the regression coefficients proposed by Liang et al. (2002).

(3*) Build-up of reflectance-to-albedo look-up-tables (LUTs*). With the pairs of simulated Landsat-like surface reflectance and surface shortwave albedo, we created LUTs of reflectance-to-albedo relations using the linear regression approach for each angular setting (He et al. 2018; Qu et al. 2013). To minimize the potential impact from Landsat satellite orbital drifts (e.g., Landsat-5 drifted between 1995-2000 and 2003-2007, Landsat-7 drifted from 2017 to the present; Qiu et al. 2021; Zhang and Roy, 2016), we trained spectral reflectance and shortwave albedo relations for local solar noon (e.g., 12:00 p.m.) geometry that is independent from instantaneous satellite observation time.

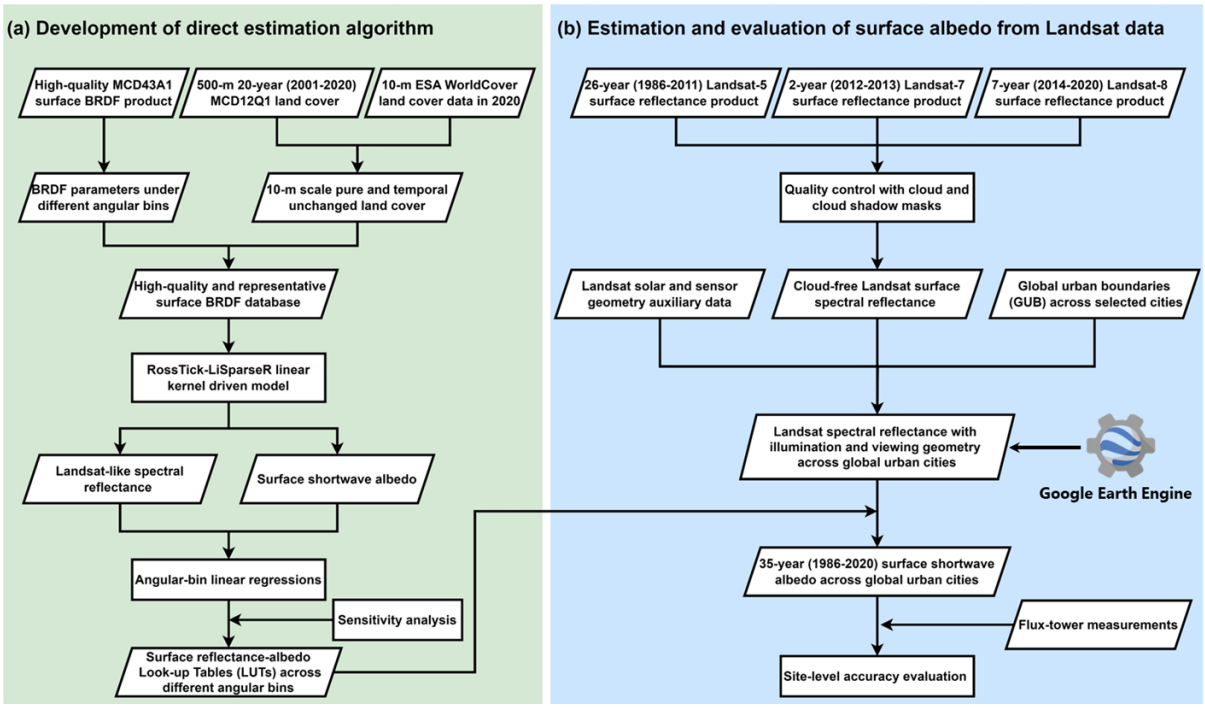

Fig. 3*. Satellite-based direct estimation of surface albedo from Landsat, with two major steps:* ***(a)*** *direct estimation algorithm development, and* ***(b)*** *surface albedo estimation and evaluation.*

We applied our reflectance-to-albedo LUTs (BSA and WSA; Eq. 1) on the Google Earth Engine (GEE, Gorelick et al. 2017) cloud-computing platform to estimate urban surface albedo for global cities using four steps. First, we used the pixel-level QA auxiliary layer to exclude cloud, cloud shadow, and snow contaminated pixels in Landsat surface reflectance. Second, we estimated BSA and WSA from the quality-controlled Landsat surface, where the solar geometry is extracted from metadata and sensor geometry is set as nadir due to small variations in Landsat sensor viewing (< 7.5°; Nagol et al. 2015). Third, we calculated annual blue-sky albedo from BSA and WSA by using the diffuse fraction (i.e., fraction of diffuse radiation in total illumination radiation) from the BaRAD dataset. Based on Landsat spectral reflectance, we also calculated the annual NDVI as an indicator of vegetation cover. Finally, we stored Landsat-derived blue-sky albedo and NDVI as two separate data layers for each city over 35 years. To verify the feasibility of the direct estimation approach with training samples from mixed land covers over urban areas, we also compared the algorithm with the training samples of pure urban cover in the discussion section.

$$\alpha = C_0(\theta_s, \theta_v, \varphi) + \Sigma^{N}_{i=1} C_i(\theta_s, \theta_v, \varphi) \times \rho_L(\lambda_i) \quad (1)$$

where α is the surface shortwave albedo (BSA and WSA); $\rho_L(\lambda_i)$ is the Landsat surface reflectance at spectral band λ_i (i = 1, 2, 3, …, N; N = 6, 6, and 7 for Landsat-5, Landsat-7, and Landsat-8, respectively); and $C_i(\theta_s, \theta_v, \varphi)$ denotes the regression coefficient at spectral band λ_i for solar zenith angle θ_s, view zenith angle θ_v, and relative azimuth angle φ.

3.2. Evaluation of urban albedo with radiation data from urban flux towers

We evaluated the accuracy and uncertainty of Landsat blue-sky albedo using observed albedo calculated from the incoming and outgoing shortwave radiation measured by 21 urban sites (**Table 2**). To match the Landsat-derived albedo at local solar noon and minimize diurnal variations (Minnis et al. 1997), we used observations from 11:00 a.m. to 1:00 p.m. local standard time. As the diffuse fraction (*d*) is not recorded by these flux tower datasets and the BaRAD dataset is too coarse for site-scale albedo calculation, we thus adopted a two-step strategy: (1) if the MODIS Aerosol product (MOD08) has high-quality Aerosol Optical Depth (AOD) observation over the target flux site, the radiative transfer simulation approach was applied (Wang et al. 2018); and (ii) otherwise, we adopted an empirical approach shown in Eq. 2 to calculate diffuse fraction *d* (Stokes and Schwartz, 1994):

$d = 0.122 + 0.85 \times \exp(-4.8 \times \cos(\theta_s))$ (2)

We used the radiation flux footprint estimated from sensor height (**Table 2**; Román et al. 2009) to crop the pixel-level Landsat blue-sky albedo image and calculate the corresponding albedo average, and then compared this Landsat blue-sky albedo average with the tower-based albedo measured on the same dates. For the accuracy assessment, four commonly used metrics were used: bias (mean difference between Landsat-derived and tower-based albedo), root-mean-square-error (RMSE), relative root-mean-square-error (rRMSE, the ratio between RMSE and the measured albedo mean), and coefficient of determination (R^2), with equations as follows:

$$Bias = \frac{1}{N}\sum_{i=1}^{N}\left(\alpha_{Landsat,i} - \alpha_{ground,i}\right) \quad (3)$$

$$RMSE = \sqrt{\frac{1}{N}\sum_{i=1}^{N}\left(\alpha_{Landsat,i} - \alpha_{ground,i}\right)^2} \quad (4)$$

$$rRMSE = \frac{RMSE}{\overline{\alpha_{ground}}} \times 100\% \quad (5)$$

$$R^2 = \frac{\sum_{i=1}^{N}(\alpha_{Landsat,i}-\overline{\alpha_{Landsat}})(\alpha_{ground,i}-\overline{\alpha_{ground}})}{\sum_{i=1}^{N}(\alpha_{Landsat,i}-\overline{\alpha_{Landsat}})^2 \sum_{i=1}^{N}(\alpha_{ground,i}-\overline{\alpha_{ground}})^2} \quad (6)$$

where $\alpha_{Landsat,i}$ and $\alpha_{ground,i}$ are *ith* Landsat-derived and ground-measured albedo; $\overline{\alpha_{Landsat}}$ and $\overline{\alpha_{ground}}$ are the average values of Landsat-derived and ground-measured albedo; *N* is the number of observations.

3.3. Spatiotemporal characteristic analysis of surface albedo in global cities

We calculated the 35-year city-scale blue-sky albedo mean from Landsat albedo time series to explore its spatial patterns. To further examine the temporal trends, we used the non-parametric Mann-Kendall statistic (Mann, 1945) and the non-parametric Theil–Sen slope estimator (Theil, 1950) approaches, which do not require specific data distribution and are robust to outliers (Wang et al. 2019), to calculate the magnitude and direction of the pixel-level monotonic albedo trend at a statistical significance level of 0.05 (i.e., *p*-value < 0.05). The city-scale albedo trend is calculated as the aggregation mean of all pixels that passed the significance test within the city area. The spatiotemporal patterns of Landsat blue-sky albedo are undertaken for two periods (1986-2020 and 2001-2020). For comparison, we extracted 35-year city-scale spatiotemporal patterns of MODIS blue-sky albedo in 2001-2020, which is calculated from the integration of MODIS BSA, WSA, and BaRAD-derived diffuse fraction.

3.4. Associations between urban greening and albedo change

We explored the multifaceted associations between urban greening and albedo change in several steps. First, the spatiotemporal patterns of Landsat NDVI in the 1986-2020 and 2001-2020 time periods were calculated and aggregated to city-level means. Second, the intra- and inter-city associations between urban albedo and NDVI trends were analyzed. Local examples in four typical cities: two rapid-urbanized Shenzhen city (22° 32′ 29.4″ N, 114° 3′ 34.56″ E), China and Birmingham city (52° 29' 10.47"N, 1° 53' 25.44"W), United Kingdom, together with two well-urbanized Milton city (30°37'49.0"N 87°02'47.0"W), Florida, and Pinehurst city (36° 41' 43" N, 119° 0' 57" W), North Carolina, United States, were selected to showcase different pathways by which urban greening modulates surface albedo during the urbanization process. Lastly, the associations between urban albedo and vegetation in 2-D (measured by NDVI) and 3-D (measured by vegetation height from 10-m-resolution Sentinel-2; Lang et al. 2023) were investigated to elucidate the effects of urban greenery on surface albedo using data at the baseline year 2020.

3.5. Urban surface radiative forcing induced by albedo change

Changes in radiative forcing can be caused by natural and/or anthropogenic drivers (Shindell et al. 2013). A positive radiative forcing occurs when there is more incoming than outgoing energy (i.e., warming), whereas a negative radiative forcing (outgoing > incoming energy) results in a cooling effect. We quantified the urban surface radiative forcing (*RF*) from albedo changes (Chen et al. 2015) using the following equation:

$RF = -K\downarrow \times (\alpha_{t2} - \alpha_{t1})$ (7)

where K↓ is the mean incoming or downward shortwave solar radiation between years t_1 and year t_2; and $\alpha_{t2} - \alpha_{t1}$ is the surface albedo difference between those years. We used BaRAD and Landsat-derived blue-sky albedo to derive pixel-scale RF (Eq. 7) and then calculated the city-scale RF from pixel-scale data. To minimize the impact of fluctuations in annual albedo, we used a 5-year average annual albedo for the RF calculation in 1986-2020. Namely, the mean surface albedo (α_{t1}) was estimated for the 1986-1990 period, and α_{t2} for the 2016-2020 period, and K↓ was estimated as the mean downward shortwave solar radiation between 1991 and 2015.

4. Results

4.1. Accuracy assessment of Landsat urban albedo

We assessed the accuracy of Landsat-derived surface albedo using the flux tower-based observations (**Table 2**). Across the 21 flux tower sites, Landsat satellites individually achieve a high albedo accuracy (bias = -0.011 - 0.005, RMSE = 0.019 - 0.026, rRMSE = 15.4% - 20.1%, R^2 = 0.58 - 0.71; **Fig. 4b-d**). For all three Landsat satellites, the overall accuracy is also reliable (bias = 0.005, RMSE = 0.025, rRMSE = 19.5%, R^2 = 0.66; **Fig. 4a**). Temporal validation for individual (**Fig. S3**) and combined (**Fig. S4**) years show similar

accuracy patterns. These assessment results suggest that the Landsat-derived albedo dataset is reliable and can be used to analyze the spatiotemporal characteristics of surface albedo of cities globally.

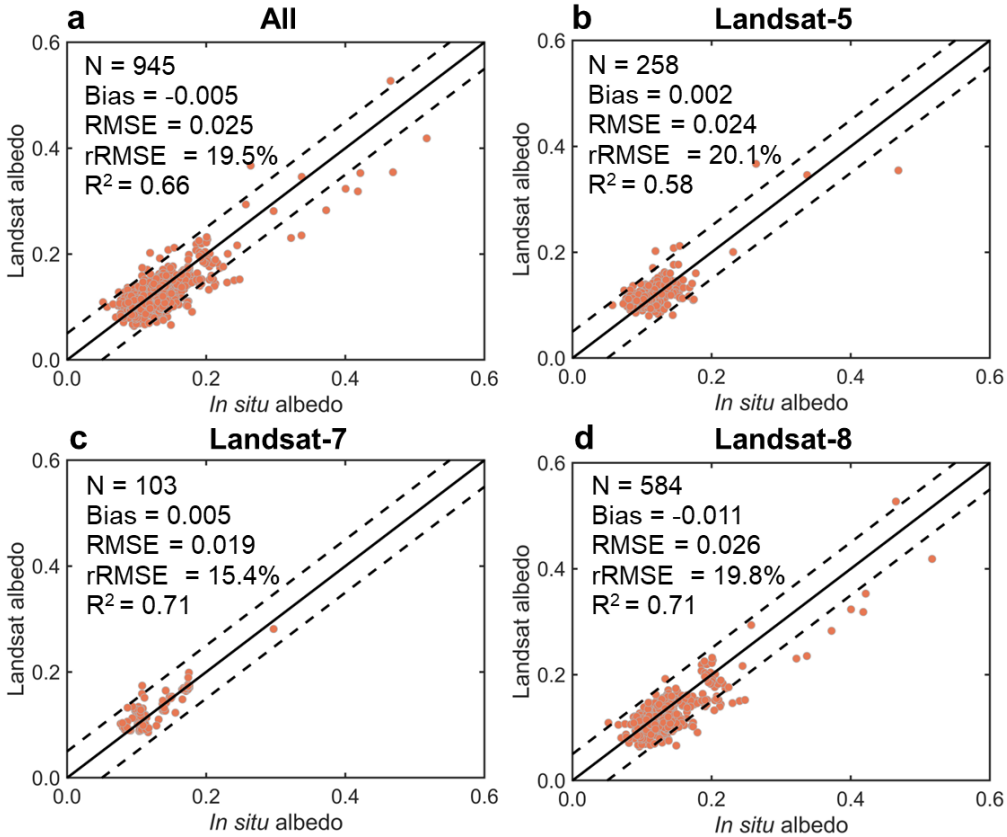

Fig. 4. *Evaluation of Landsat-derived albedo with flux-tower measurements for* ***(a)*** *all three Landsat satellites,* ***(b)*** *Landsat-5,* ***(c)*** *Landsat-7, and* ***(d)*** *Landsat-8. The following comparison statistics are calculated: N (number of Landsat data observed on the same date as flux-tower measurements), bias (mean difference between Landsat-derived and tower-based albedo), RMSE (root-mean-square-error), rRMSE (relative RMSE, ratio between RMSE and measured albedo mean) and R^2 (coefficient of determination), 1:1 line (solid line), error lines of -0.05 and 0.05 (dashed line).*

4.2. Global variations of urban albedo

The 35-year (1986-2020), city-wide mean surface albedos for the 3037 global cities assessed here have clear spatial patterns (**Fig. 5**). Cities in temperate climates have the lowest mean albedo (0.143, N = 1340), followed by those in cold (0.144, N = 1073), tropical (0.145, N = 161), and arid (0.174, N= 463) regions. Cloud cover limits the number of tropical cities meeting the threshold of having 35-year data. The albedo range for tropical cities (0.115-0.240) is in line with the range reported by Rechid et al (2009) (0.10-0.20). The urban albedo distribution is skewed, with most cities (2452) within the range of 0.12-0.16, followed by 462 cities within the range of 0.16-0.20, 87 cities with albedos > 0.2, and only 36 cities < 0.12. The 20-year (2001-2020) city-level annual mean albedo from the MODIS and Landsat datasets are close to those of the 35-year Landsat equivalence (**Fig. S5**), with the majority of cities within the range of 0.12-0.20 and very few presenting albedos <0.12 or > 0.20.

4.3. Global variations of urban albedo trend and driver attribution

4.3.1. Global temporal trends of urban albedo

The 35-year (1986-2020) trend of city-scale annual mean surface albedo depicts a negative slope of -0.0007 yr^{-1} (**Fig. 6**). When cities are subdivided by their mean trend, 2921 shows a decreasing trend (mean trend = -0.0007 yr^{-1}) and 116 an increasing trend (mean trend = 0.0004 yr^{-1}). Rapid changes, lower than -0.001 yr^{-1}, were observed in 312 cities across Europe, North America, East Asia, and the Middle East. Most cities are in the -0.001 – 0.000 yr^{-1} (2609) and 0.000 to 0.001 yr^{-1} (107) albedo change rate. Nine cities with a larger increasing albedo trend (> 0.001 yr^{-1}) were observed in the Southwest region of the United States.

The 21-year (2000-2020) trends for MODIS and Landsat consistently decrease (**Figs. S6**), at rates of -0.0003 yr^{-1} and -0.0014 yr^{-1}, respectively. Due to its inability to detect fine-scale urban heterogeneity, the 500-m-resolution MODIS satellite returns a lower decreasing rate than the 30-m-resolution Landsat (**Fig. S7**), supporting the necessity of using high-resolution satellite data to monitor urban environments. The 21-year change rate (-0.0014 yr^{-1}) is twice as high as the 35-year trend (-0.0007 yr^{-1}) for Landsat, indicating that the rate of worldwide urban albedo decrease has grown.

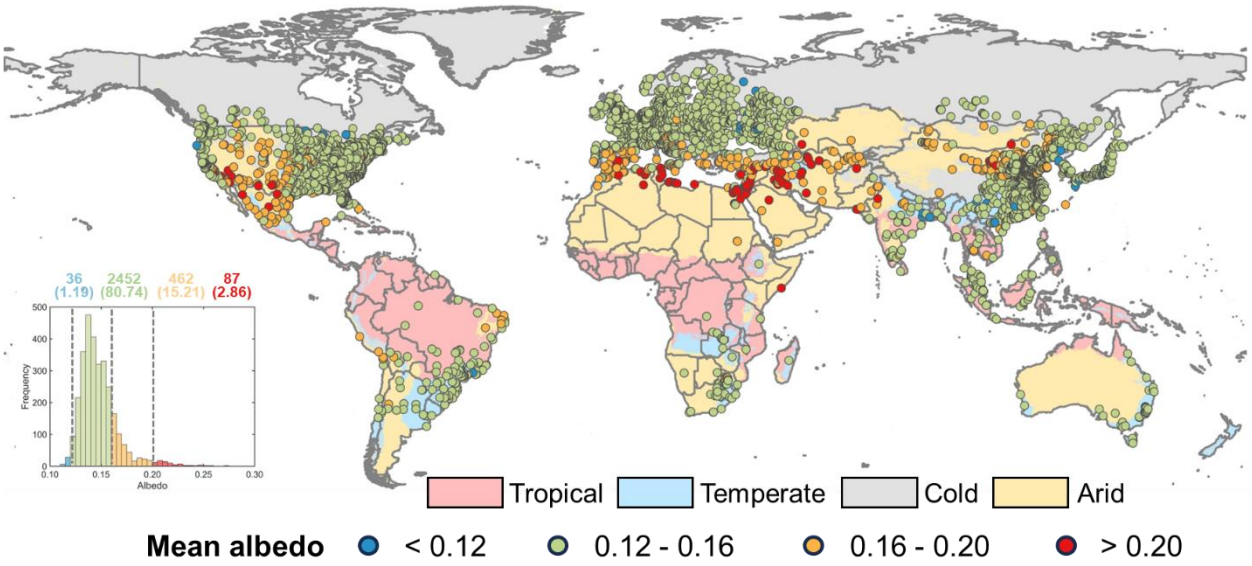

***Fig. 5**. City-level average annual albedo (lower key) derived from 35-year (1986-2020) Landsat data for 3037 global cities mapped onto 1-km Köppen-Geiger climate (Beck et al. 2018) (upper key), with the number of cities (and the associated percentage in parentheses) given above the inserted histogram.*

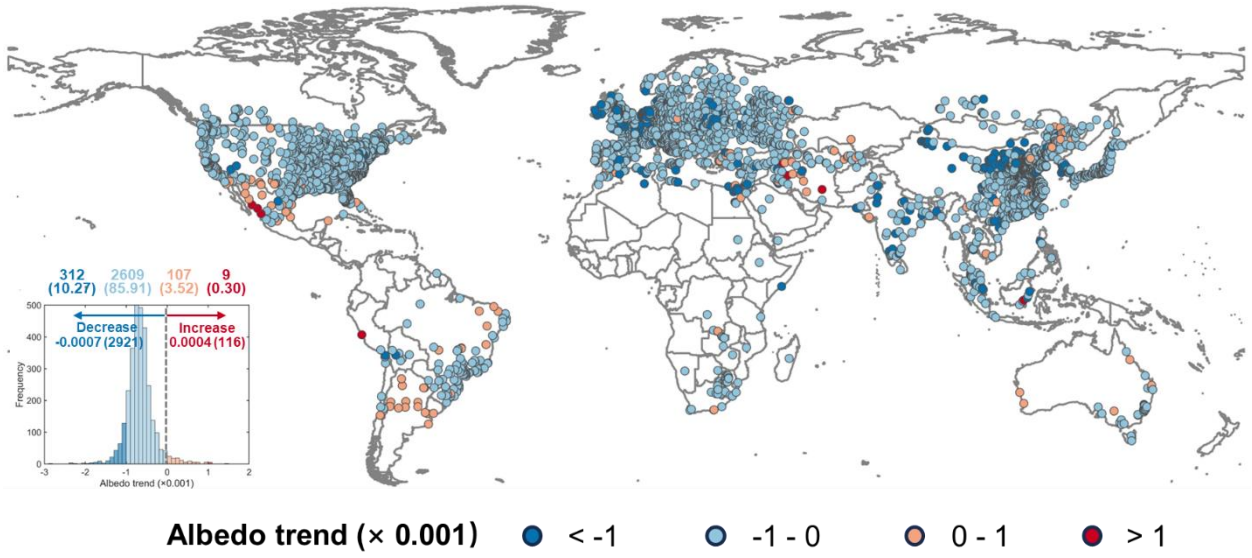

***Fig. 6**. Spatial patterns of the Landsat-derived city-level albedo trend for 3037 global cities over 35 years (1986-2020), with the albedo trend histogram and the number of cities (with the related percentage in parentheses) given above the inserted histogram.*

4.3.2. Associations between urban albedo and greenness

Greening activity is one potential driver influencing urban albedo change. Landsat NDVI has a mean increase of 0.001 yr^{-1} for these 3037 cities during the same 35-year period, with 2205 cities exhibiting an increase (i.e., greening) and 832 experiencing a decrease (i.e., browning, **Fig. 7**). Most cities are in the 0.000 to 0.003 yr^{-1} (1742) and -0.003 to 0.000 yr^{-1} (642) NDVI change range, followed by 463 cities with an increasing NDVI trend > 0.003 yr^{-1} and 190 cities with a decreasing NDVI trend < -0.003 yr^{-1}. Browning cities are predominantly found in East Asia, South America, and the Southwest region of the United States.

Intra-city associations (within cities) between urban NDVI and albedo trends show a total of 2564 cities are negatively correlated (**Fig. 8**), with 583, 1077, and 904 cities presenting correlation coefficients < -0.6, within the -0.6 to -0.3, and -0.3 to 0 ranges, respectively. Only 291 of 473 cities have statistically significant positive NDVI-albedo relationships, most of which are distributed in Europe and East Asia. Inter-city associations (across cities) using the median albedo trends derived from 10% NDVI bins show that the increase in NDVI trend (with a slope of -0.049) coexists with the decrease in albedo trend, which explains 92% of the total variance of the albedo binned trend (**Fig. 9a**). Moreover, statistical results of NDVI and albedo trend consistency from the raw observations show a decrease in albedo trend of 2176 (71.65%) cities in the opposite direction with respect to the NDVI trend (**Fig. 9b**). As the greening trend is greater (0.004 yr^{-1}) for the past 21 years (**Fig. S8**), the intra- and inter-city associations between urban NDVI and albedo trends become stronger, with more cities exhibiting negative NDVI-albedo correlation coefficients (**Figs. S9 and S10**). These intra- and inter-city dominant negative associations reveal that urban greening will lead to a decreasing albedo trend.

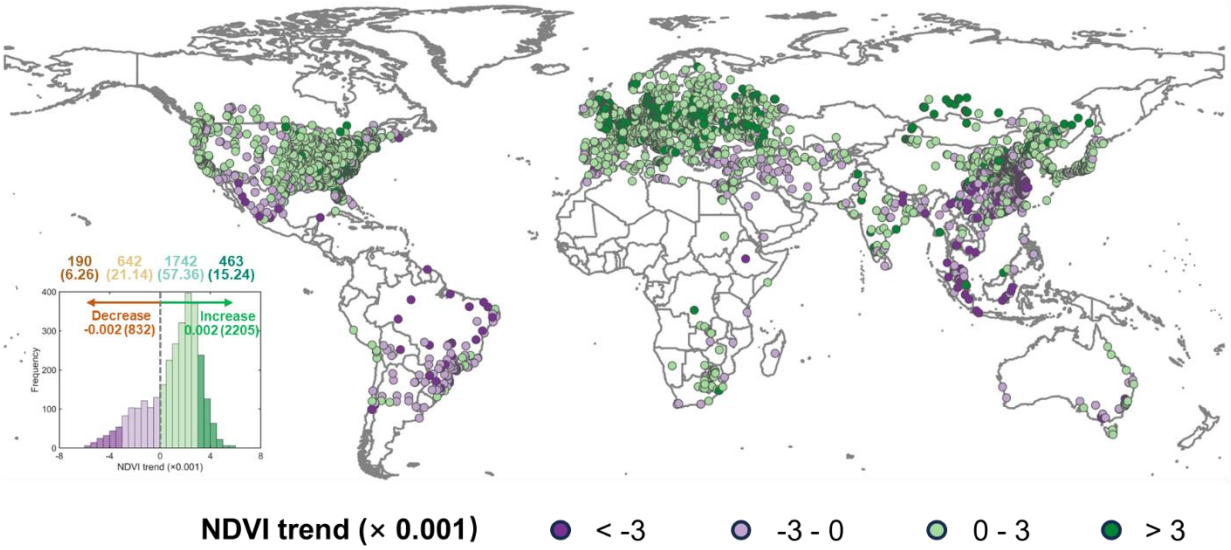

***Fig. 7**. Spatial patterns of the Landsat-derived city-level normalized difference vegetation index (NDVI) trend for 3037 global cities over 35 years (1986-2020), with the NDVI trend histogram and the number of cities (with the related percentage in parentheses) given above the inserted histogram.*

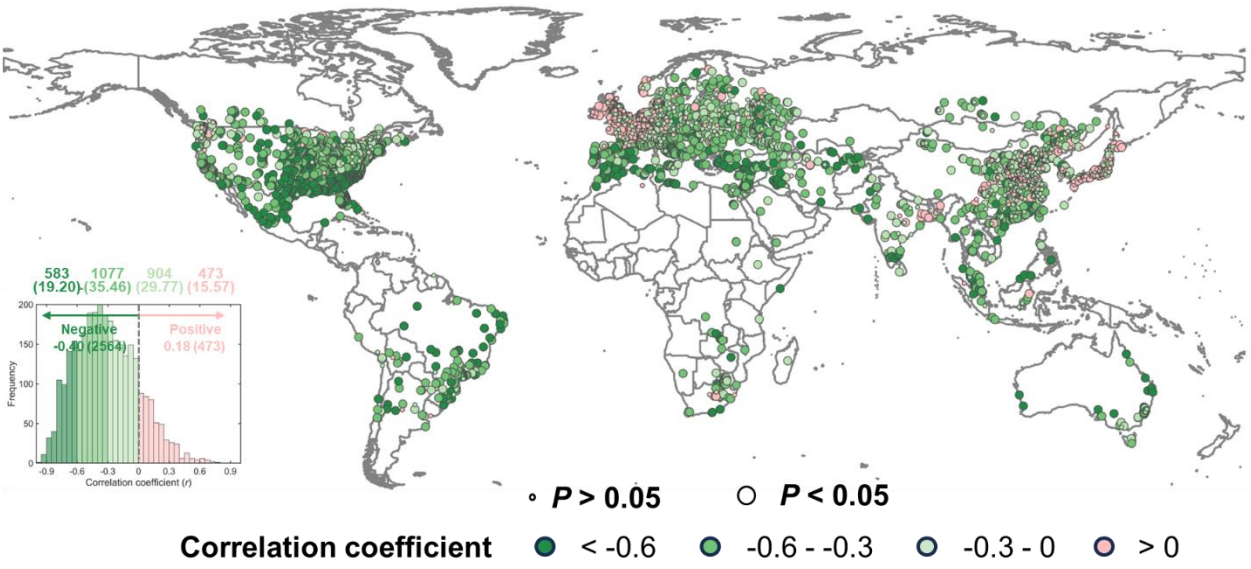

***Fig. 8**. Spatial patterns of the intra-city correlation between urban normalized difference vegetation index (NDVI) and albedo trend for 3037 global cities over 35 years (1986-2020), with the histogram (correlation coefficient key) of the city-level albedo trend and the number of cities (with the associated percentage in parentheses) given above the inserted histogram. Large markers represent a statistical significance level of 0.05 (p-value <0.05) and small markers represent a non-significant trend with p-value >0.05.*

Four sample cities provide spatially explicit information on the decreasing trend of surface albedo caused by different greening pathways: tree planting (Shenzhen, China and Birmingham, United Kingdom) and urban warming-induced vegetation growth (Milton, Florida and Pinehurst, North Carolina, United States). Shenzhen and Birmingham have experienced tremendous urbanization during the past three decades, but they have also implemented tree planting programs in central areas, as it can be observed through the NDVI trend maps and high-resolution Google Earth satellite images (**Fig. 10a-c** and **Fig. 11a-c**). Two local sites in both Shenzhen and Birmingham clearly show the opposite trends for the NDVI and albedo time series (**Fig. 10d-e** and **Fig. 11d-e**). In comparison, Milton and Pinehurst are two well-urbanized cities without substantial impervious area expansion in the urban fringe areas. Despite the absence of large-area tree planting activities, greenness continues to increase in these two cities due to enhanced vegetation growth induced by urban warming (**Figs. 12** and **13**). The significant negative correlation between surface albedo and 2-D (NDVI as vegetation coverage) and 3-D (vegetation height) vegetation structure metrics in the baseline year 2020 further explains the multifaceted controls of urban greening on surface albedo (**Fig. 14**). Besides urban greening, the other anthropogenic practices might influence surface albedo variations. For example, as shown in **Figs. S11** and **S12**, building construction and rooftop renewal with new light-color materials increase surface albedo. Nevertheless, the frequency and intensity of building construction is lower than urban vegetation growth, which results in the greening-dominated declining trend of urban surface albedo worldwide.

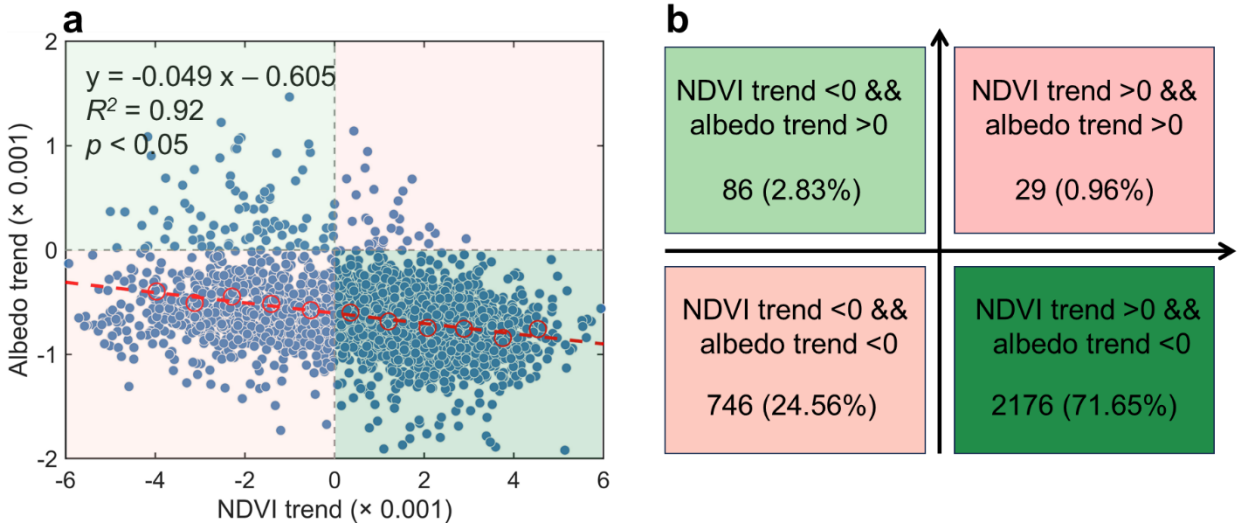

Fig. 9. *Associations between city-level normalized difference vegetation index (NDVI) and surface albedo trends for 3037 global cities over 35 years (1986-2020), with* ***(a)*** *scatter plot and* ***(b)*** *statistics of NDVI and albedo trend consistency. In* ***(a)****, the city-level trends are averaged from pixel-level trends that are statistically significant at a level of 0.05, using the non-parametric Mann-Kendall and Theil–Sen slope estimator approaches. A zonal analysis is used to refine the association results by averaging the NDVI and albedo trend pairs (red circles) within each 10% NDVI interval for the linear regression (red dashed line).*

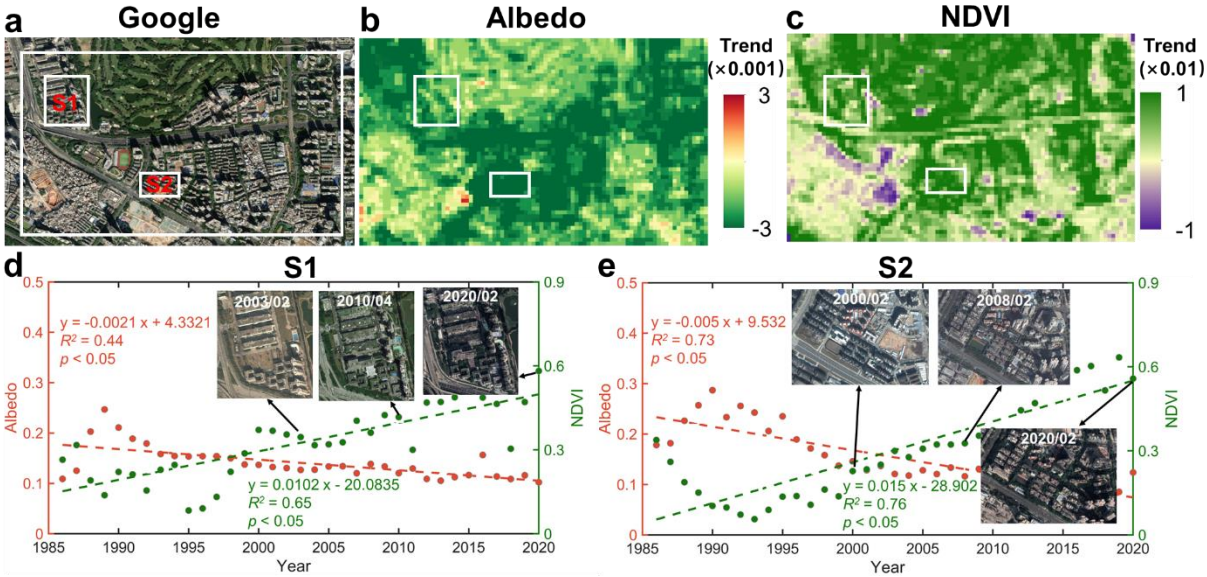

Fig. 10. *Examples showing the close association between surface albedo and urban greening in the Shenzhen city, China, based on the maps of* ***(a)*** *Google Earth satellite image,* ***(b)*** *albedo trend,* ***(c)*** *NDVI trend,* ***(d)*** *time series of urban NDVI and albedo for* ***S1*** *area in* ***(a),*** *and* ***(e)*** *time series of urban NDVI and albedo for* ***S2*** *area in* ***(a)****.*

4.4. Global variations of albedo-induced urban surface radiative forcing

The 35-year change in surface albedo has caused a mean positive surface radiative forcing of 2.76 ± 1.92 W·m^{-2} for the 3037 global cities assessed in this study (**Fig. 15**), suggesting a net increase in absorbed incoming solar energy at the urban surface. Large inter-city spatial variabilities are observed, with values ranging from -10.75 to 23.34 W·m^{-2}. The 2936 cities with positive radiative forcing (i.e., warming) have a mean value of 2.92 W·m^{-2}, while the 101 cities with negative radiative forcing have a mean value of -1.97 W·m^{-2}. The mean magnitude of albedo-induced radiative forcing also varies by regions: 3.14 W·m^{-2} for 1073 Asian cities; 3.09 W·m^{-2} for 92 African cities; 2.72 W·m^{-2} for 933 European cities; 2.60 W·m^{-2} for 789 North American cities; 1.23 W·m^{-2} for 31 Australian cities; and 0.85 W·m^{-2} for 119 South American cities.

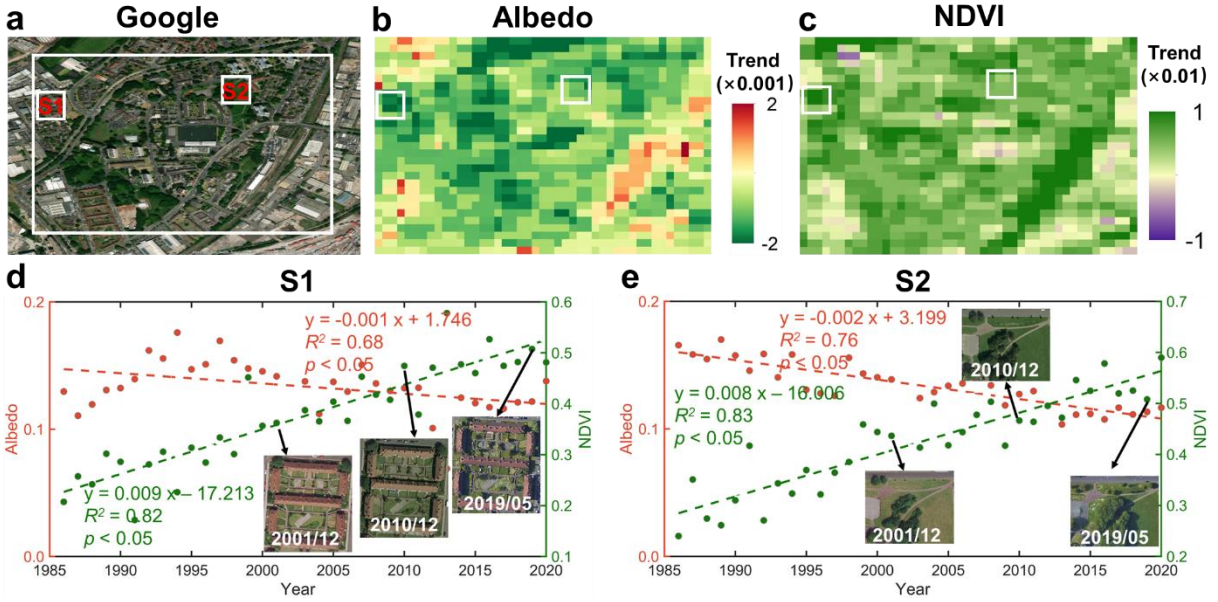

Fig. 11. *Examples showing the close association between surface albedo and urban greening in the Birmingham city, United Kingdom, based on the maps of* ***(a)*** *Google Earth satellite image,* ***(b)*** *albedo trend,* ***(c)*** *NDVI trend,* ***(d)*** *time series of urban NDVI and albedo for* ***S1*** *area in* ***(a),*** *and* ***(e)*** *time series of urban NDVI and albedo for* ***S2*** *area in* ***(a)****.*

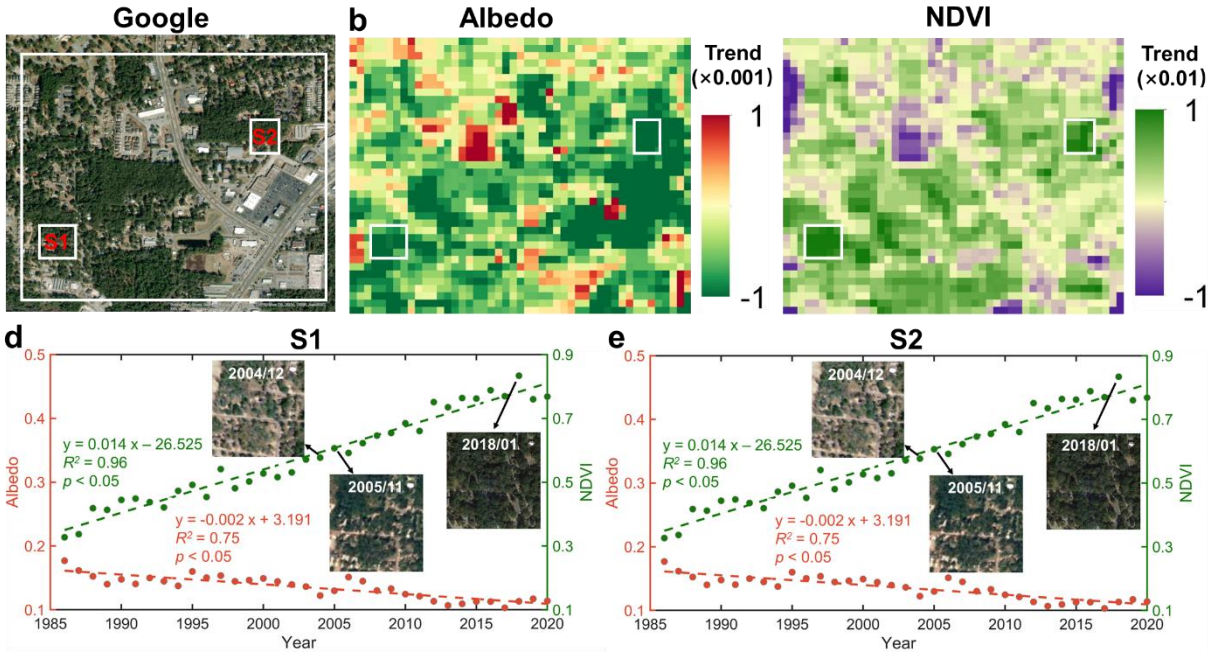

Fig. 12. *Examples of close association between surface albedo and urban greening in the Milton city, Florida, United States, based on the maps of* ***(a)*** *Google Earth satellite image,* ***(b)*** *albedo trend,* ***(c)*** *NDVI trend,* ***(d)*** *time series of urban NDVI and albedo for the* ***S1*** *area in* ***(a),*** *and* ***(e)*** *time series of urban NDVI and albedo for the* ***S2*** *area in* ***(a)****.*

5. Discussion

5.1. Uncertainty analysis

Some influencing factors such as training sample representativeness, Landsat data uncertainty, seasonal variation, building footprint, and snow event may mislead our findings. To examine their impacts, we conducted sensitivity analyses and discussed the potential uncertainties associated with each of these factors.

5.1.1. Training sample representativeness

The representativeness of training samples, angular-bin size, and regression relationship between reflectance and albedo are three factors that need to be considered for the successful application of the direct estimation approach. Recent studies have thoroughly investigated the sensitivity to the angular-bin size and the regression relationship between reflectance and albedo, verifying their applicability to both natural and urban surfaces (Chen et al. 2023; Lin et al. 2022). Therefore, training dataset representativeness has been highlighted as a key component for the application of the direct estimation approach over urban areas. We conducted two sensitivity analyses using BRDF/albedo over mixed land covers (16 IGBP land covers used in this study, referred to as general scheme) and pure urban cover (referred to as urban scheme) to test the theoretical accuracy of this approach over urban areas. Results

show that these two schemes have almost the same theoretical accuracy (0.0161 vs. 0.0156, **Fig. S13**), which is very close to the MODIS BRDF/albedo product accuracy (Wang et al. 2018). Based on the optimized BRDF/albedo training samples for the general scheme (7200 samples for 16 land covers with 450 samples per type) and urban scheme (3000 urban cover samples), we constructed one general and one urban reflectance-to-albedo LUT and validated their accuracy with global flux tower-based measurements. Validation results reveal that these two algorithms are highly accurate, suggesting that the direct estimation approach used in this study with the general training sample scheme is stable (**Fig. 4 vs. Fig. S14**).

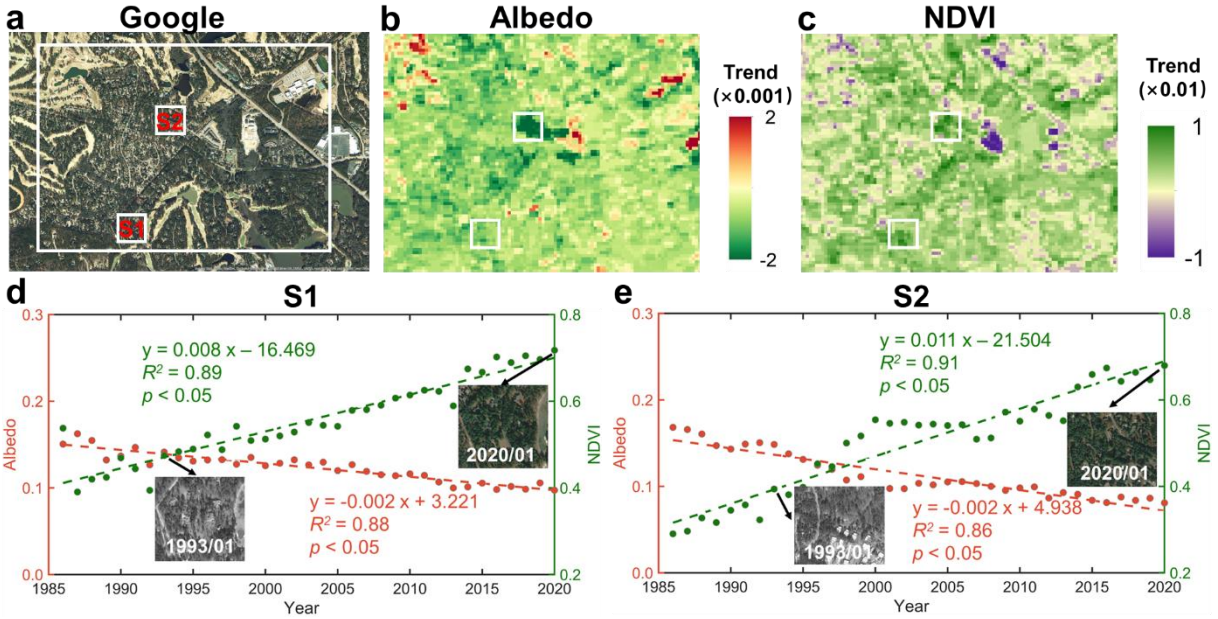

Fig. 13. *Examples of close association between surface albedo and urban greening in the Pinehurst city, North Carolina, based on the maps of* ***(a)*** *Google Earth satellite image,* ***(b)*** *albedo trend,* ***(c)*** *NDVI trend,* ***(d)*** *time series of urban NDVI and albedo for the* ***S1*** *area in* ***(a),*** *and* ***(e)*** *time series of urban NDVI and albedo for the* ***S2*** *area in* ***(a)****.*

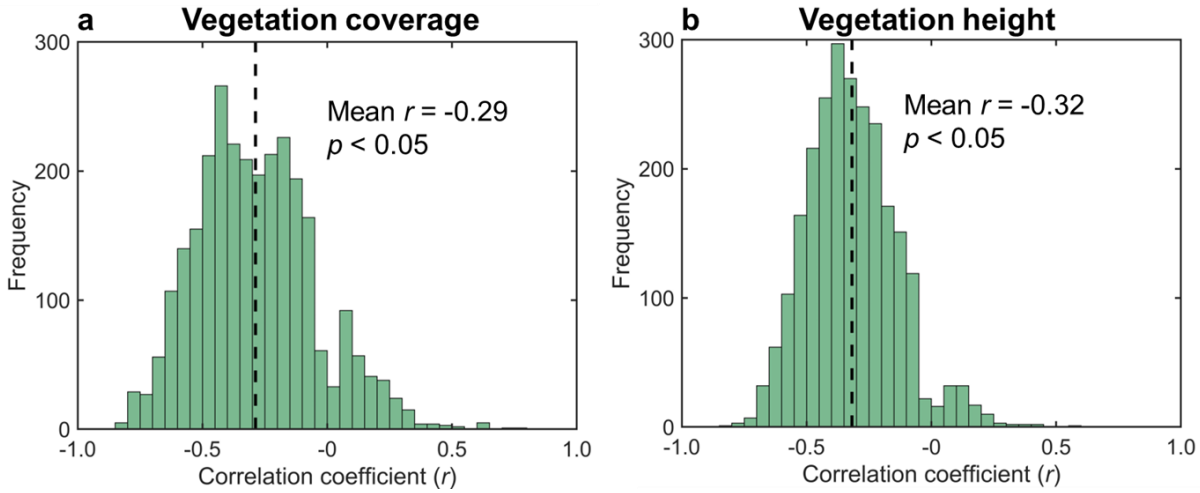

Fig. 14. *Correlation between surface albedo and* ***(a)*** *30-m-resolution Landsat normalized difference vegetation index (NDVI, Gorelick et al. 2017), and* ***(b)*** *10-m-resolution vegetation height (Lang et al. 2023) of the baseline year 2020 for 3037 global cities.*

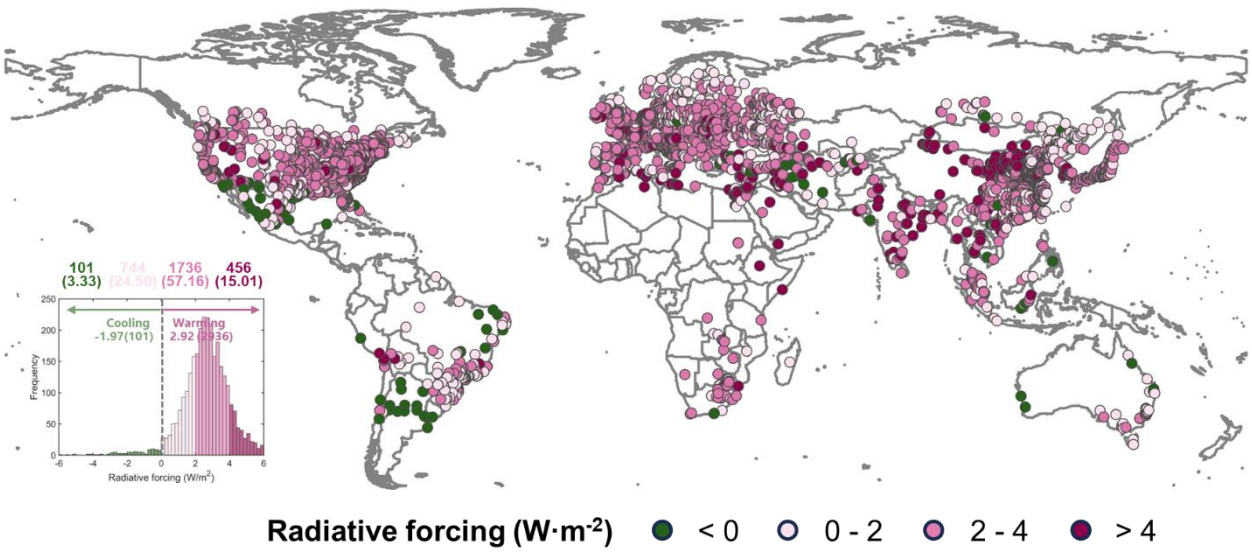

Fig. 15*. Spatial patterns of surface radiative forcing (RF, W•m^{-2}) from albedo change for 3037 global cities over 35 years (1986-2020), with the number of cities (and the associated percentage in parentheses) given above the inserted histogram.*

5.1.2. Landsat data uncertainty

The uncertainty of Landsat data quality mainly stems from Landsat satellite orbital drifts and scan line corrector (SLC) failure in Landsat-7. On the one hand, Landsat satellite orbital drifts (e.g., Landsat-5 drifted between 1995-2000 and 2003-2007, Landsat-7 drifted from 2017 to the present; Qiu et al. 2021; Zhang and Roy, 2016) alter local acquisition time, affecting solar-viewing geometry and surface reflectance, resulting in artificial impacts on surface albedo. To minimize such impacts, we trained the spectral reflectance with shortwave albedo at local solar noon (e.g., 12:00 p.m.) to construct reflectance-to-albedo LUTs, allowing us to compare predicted surface albedo across years (Guo et al. 2022). On the other hand, since Landsat-7 data covers only two years (2012-2013), the data gap impacts from this satellite on the main findings of this study are minor. Sensitivity analysis shows that the yearly mean and long-term temporal trend of global urban albedo are nearly the same, whether or not Landsat-7 satellite data are used (**Figs. 5-6** vs. **Fig. S15**).

5.1.3. Seasonal variation

Seasonal impacts on urban albedo estimation and analysis come from two sources: seasonal vegetation growth and seasonal solar geometry change. On the one hand, Landsat satellite has a regular 16-day revisit cycle, which allows at least two observations per month to capture seasonal vegetation growth dynamics. On the other hand, our algorithm has normalized surface albedo to local solar noon and the solar position is relatively stable within a month, minimizing the interference from seasonal change of solar geometry. Sensitivity analysis results of the Landsat-derived albedo trends using time series from different seasons are very similar to those of the annual mean time series (**Fig. S16**), supporting the minor seasonal variation effects on the observed decreasing albedo trend of global urban cities in this study.

5.1.4. Building footprint

Building footprint changes, such as those related to new construction or building renovations using different materials, might increase urban albedo (**Figs. S11** and **S12**). To explore building footprint impacts on surface albedo, we used 30-m-resolution rasterized building footprint (i.e., total, average, minimum, and maximum building areas within a 30-m-resolution pixel) dataset for 242 cities in the United States (Heris et al. 2020), and three building height datasets for China (120 cities; Yang and Zhao et al. 2022), Germany (18 cities; Frantz et al. 2021), and the United States (372 cities; Falcone, 2016) to provide the horizontal and vertical building footprint metrics (**Table S2**). By conducting a bivariate relationship analysis between building footprint metrics and albedo, we found a positive correlation with mean correlation coefficients of 0.21, 0.21, 0.21, and 0.16 for maximum (i.e., area of the largest building intersecting each 30-m pixel), minimum (i.e., area of the smallest building intersecting each 30-m pixel), average (i.e., number of buildings that intersect each 30-m pixel), and total (i.e., total building footprint coverage per 30-m pixel) building areas, respectively (**Fig. S17**). We also observed a negative correlation between albedo and building height, with a mean correlation coefficient of -0.22 (**Fig. S18**), as shadowing and radiative trapping in canyons increase with building height. However, quantifying the contribution of the building landscape to albedo change remains a challenging task due to the lack of high-resolution urban building time-series products, which requires future investigation.

5.1.5. Snow cover impact

Snow cover is another important confounding factor for the spatiotemporal analysis of global urban albedo due to its much higher reflectance than other urban materials. On one hand, because regular snow events only occur for short periods in the winter for high-latitude cities, they will have little impact on the general diminishing patterns of global urban albedo. Snow episodes, on the other hand, are rather regular across time, and their influence on long-term urban albedo is likely to be systematically linear, which will not modify the spatiotemporal trend analysis. Our sensitivity analysis results demonstrate that, with the exception of a few high-latitude Northern hemisphere cities, the overall decreasing trends of worldwide urban albedo are nearly the same whether snowy satellite pixels are excluded or not (**Fig. 6** and **S19**).

5.2. Novelty and implication of this study

This study makes several advances over past similar studies on methodological development. First, we investigated the direct estimation approach and validated its theoretical capability for retrieving surface albedo from Landsat over global urban areas. Our training sample representativeness sensitivity analyses indicate that more accurate urban BRDF/albedo training datasets beyond MODIS are one potential way to improve the algorithm accuracy, which should include fine-resolution 3-D radiative transfer model parameterization and global 3-D urban morphology datasets. Second, the absolute accuracy of the direct estimation approach for estimating urban albedo had not yet been properly evaluated. For the first time, this study used albedo data from incoming and outgoing shortwave radiation measured by synthesized global urban flux towers around the world as ground truth to assess the accuracy of the proposed algorithm. The results demonstrated that Landsat-derived urban albedo is reliable (**Fig. 4**).

The global 35-year, 30-m-resolution urban surface albedo dataset generated in this study is unique and valuable. Although many previous efforts have attempted to estimate surface albedo from high-resolution Sentinel-2 and Landsat satellite data (Guo et al. 2022; He et al. 2018; Lin et al. 2022; Shuai et al. 2011; 2014), most of them were limited to individual locations, cities, or specific regions, and years, which hampered our understanding of the spatiotemporal patterns of global urban albedo throughout the past three decades of urbanization. Our albedo dataset of 3037 cities from around the world, including cities in the Global North and Global South, provides us a thorough picture of the dynamic spatiotemporal evolution of global urban albedo. This dataset can be incorporated as input data into urban canopy models (Ryu et al. 2016) for the monitoring and estimation of urban energy balance and other albedo-related studies.

By comparing the results of the previous three decades with those of the previous two decades using the global 30-m resolution Landsat albedo dataset developed here, we found that global urban albedo is decreasing at an increasing rate, implying that the albedo-induced warming has been exacerbated. We also observed that the urban greening phenomenon is expanding around the globe. Since 1985, 72.60% of global cities (2205) have increased greening, and this proportion has increased to 89.20% (2709 cities) since 2001. This proportion is higher than the 70% reported in a previous study using coarse-resolution MODIS data (Zhang et al. 2021). Finally, our study demonstrates that urban greening regulates the decreasing trend of urban albedo through two different pathways: tree planting and urban warming-enhanced vegetation growth. These findings help to clarify recent controversial conclusions about worldwide urban albedo trend patterns (Guo et al. 2022; Ouyang et al. 2022). Guo et al. (2022) reported an increasing trend of urban albedo based on 30-m resolution Landsat-derived summer albedo across 11 Chinese megacities, without taking into account the various urbanization trends in other Chinese cities or around the world, as well as seasonal changes. By comparing the 1°-resolution albedo estimated from MODIS land cover types across two baseline years, 2018 and 2001, Ouyang et al. (2022) found a decreasing pattern in urban areas. This coarse-resolution and short-term data (since 2001) cannot detect fine-scale heterogeneity in the urbanization processes during the past three decades, such as tree planting and construction of new buildings and roads, as well as changes in existing artificial impervious surfaces. Using our 30-m resolution surface albedo and NDVI dataset covering 3037 cities around the world, we determined that greening is the key controlling factor for the downward trend of urban albedo using multidimensional association analysis and further evidence from local cases.

The strong relationship between urban greening and albedo has important implications. Planting trees, in conjunction with artificial albedo alterations (e.g., the use of high-reflective materials), have been recognized as two critical approaches to mitigate urban warming (Chen et al. 2022; Wong et al. 2021). However, albedo-induced warming effects of urban greening have received little attention. Recent vegetation greening research at regional and global scales have found that albedo is a key component in the greening-induced change in the Earth's energy budget and might potentially offset cooling benefits, causing local and global warming (Lian et al. 2022; Piao et al. 2020). This study provides empirical evidence of the warming effect triggered by changes in urban albedo caused by increased vegetation, a phenomenon that must be taken into account when evaluating the effectiveness of greening-based cooling solutions by incorporating such fine-scale datasets with 3-D microclimate models (e.g., SOLWEIG; Lindberg et al. 2008).

5.3. Limitations and future perspectives

It is important to recognize and resolve various limitations and uncertainties in this study for future research. Topography is an essential factor in estimating albedo, although it has seldom been taken into account when mapping surface albedo on a wide scale using satellite data. In this study, we do not include topography, as the majority of the cities investigated exhibit minimal variations in elevation (mean slope = 3.3°, **Fig. S20**). But some cities have large slopes, and their surface albedo retrieval may still require accounting for topographic impacts (Wu et al. 2018, 2019).

Another critical issue to address is 3-D urban morphology, which requires significantly higher resolution data (e.g., ~1 m) for both the satellite surface reflectance and morphology datasets. The impact of urban geometry, such as the density of buildings, the sky view factor, and the aspect ratio of buildings, on surface albedo, and in turn on air temperature close to the surface is widely recognized (Xu et al. 2020; Yang and Li, 2015). The increasing availability of high-resolution Digital Surface Model data (e.g., Scott et al. 2022) and 3-D building data (e.g., Zhou et al. 2022) will strengthen interpretation of higher-resolution satellite observations beyond Landsat (e.g., 10-m Sentinel-2 with ~5-day revisit; 3-m PlanetScope with daily revisit; Drusch et al. 2012; Planet Team, 2022) to improve albedo estimates at urban facet scale (e.g., road, roof, and wall).

Although fine-scale albedo trends have been studied, Landsat data remains a mixed signal that cannot effectively segregate individual contributions from different urban elements (e.g., building, tree, and grassland) to the overall spatiotemporal trend of urban albedo. Furthermore, the individual contributions of tree planting and urban warming-enhanced vegetation growth to greening-induced urban

albedo modification are still unknown. An integration of fine-resolution land-cover datasets of different urban elements and high-resolution albedo datasets are expected to be used for isolating and assessing the individual contributions of particular urban features. Finally, this study did not take into account the detailed spatial and temporal variations associated with land cover changes, which can be analyzed by combining our Landsat albedo data with the appropriate high-resolution annual land cover map data. This will be helpful for city climate change management to address mitigation, adaptation, and forecasting because it directly affects surface energy balance (Duveiller et al. 2018; Oke 1982).

6. Conclusions

The spatial and temporal features of urban surface albedo in cities around the world and their underlying drivers are still not well understood due to a lack of high-resolution albedo observations. In this study, we generated a 35-year, 30-m resolution annual albedo dataset for 3037 worldwide cities. We demonstrated the accuracy and reliability of the albedo dataset by comparing it to albedo data derived from flux tower-based measurements. We investigated the spatial and temporal patterns and trends of urban albedo using this dataset and found that most cities had a decreasing albedo trend as a consequence of increased greenness. Cities with this decrease in albedo are expected to experience more (positive) surface radiative forcing.

Acknowledgments: This work was supported by the Open Fund of State Key Laboratory of Remote Sensing Science under Grant No. OFSLRSS202017 awarded to S.W. X. L. was supported by the Chinese National Natural Science Foundation Project (#41901290). Q.L. was supported by the Major Key Project of Pengcheng Laboratory. B.C. was supported by The University of Hong Kong HKU-100 Scholar Fund and Seed Fund for Strategic Interdisciplinary Research Scheme. The Landsat surface reflectance and MODIS BRDF/albedo product are available from the Google Earth Engine (GEE) cloud-computing platform. The Urban-PLUMBER flux tower datasets are available from https://doi.org/10.5281/zenodo.6590886. The URBANFLUXES flux tower datasets are available from http://urbanfluxes.eu/. The monthly BaRAD solar radiation dataset is available from https://doi.org/10.1594/PANGAEA.932924. The authors would like to thank all PIs of urban flux towers providing valuable flux datasets.

Data and code availability: Data and Code will be made available on request.

References

Akbari, H., Matthews, H.D., Seto, D. 2012. The long-term effect of increasing the albedo of urban areas. Environmental Research Letters, 7, 024004

Beck, H.E., Zimmermann, N.E., McVicar, T.R., Vergopolan, N., Berg, A., Wood, E.F. 2018. Present and future Köppen-Geiger climate classification maps at 1-km resolution. Scientific Data, 5, 1-12

Bjorkegren, A., Grimmond, C.S.B., Kotthaus, S., Malamud, B. 2015. CO2 emission estimation in the urban environment: Measurement of the CO2 storage term. Atmospheric Environment, 122, 775-790

Bonafoni, S., Sekertekin, A. 2020. Albedo retrieval from Sentinel-2 by new narrow-to-broadband conversion coefficients. IEEE Geoscience and Remote Sensing Letters, 17, 1618-1622

Buchhorn, M., Lesiv, M., Tsendbazar, N.-E., Herold, M., Bertels, L., Smets, B. 2020. Copernicus global land cover layers—collection 2. Remote Sensing, 12, 1044

Cao, C., Lee, X., Liu, S., Schultz, N., Xiao, W., Zhang, M., Zhao, L. 2016. Urban heat islands in China enhanced by haze pollution. Nature Communications, 7, 1-7

Chakraborty, T., Lee, X. 2021. Using supervised learning to develop BaRAD, a 40-year monthly bias-adjusted global gridded radiation dataset. Scientific Data, 8, 1-10

Chen, B., Wu, S., Song, Y., Webster, C., Xu, B., Gong, P. 2022. Contrasting inequality in human exposure to greenspace between cities of Global North and Global South. Nature Communications, 13, 1-9

Chen, H., Lin, X., Sun, Y., Wen, J., Wu, X., You, D., Cheng, J., Zhang, Z., Zhang, Z., Wu, C. 2023. Performance Assessment of Four Data-Driven Machine Learning Models: A Case to Generate Sentinel-2 Albedo at 10 Meters. *Remote Sensing*, 15, 2684

Chen, X., Liang, S., Cao, Y., He, T., Wang, D. 2015. Observed contrast changes in snow cover phenology in northern middle and high latitudes from 2001–2014. Scientific Report, 5, 1-9

Chow, W. 2017. Eddy covariance data measured at the CAP LTER flux tower located in the west Phoenix, AZ neighborhood of Maryvale from 2011-12-16 through 2012-12-31

Christen, A., Vogt, R. 2004. Energy and radiation balance of a central European city. International Journal of Climatology: A Journal of the Royal Meteorological Society, 24, 1395-1421

Chrysoulakis, N., Grimmond, S., Feigenwinter, C., Lindberg, F., Gastellu-Etchegorry, J.-P., Marconcini, M., Mitraka, Z., Stagakis, S., Crawford, B., Olofson, F. 2018. Urban energy exchanges monitoring from space. Scientific Report, 8, 1-8

Coutts, A.M., Beringer, J., Tapper, N.J. 2007. Characteristics influencing the variability of urban CO2 fluxes in Melbourne, Australia. Atmospheric Environment, 41, 51-62

Crawford, B., Christen, A. 2015. Spatial source attribution of measured urban eddy covariance CO2 fluxes. Theoretical and Applied Climatology, 119, 733-755

Crawford, B., Grimmond, C., Christen, A. 2011. Five years of carbon dioxide fluxes measurements in a highly vegetated suburban area. Atmospheric Environment, 45, 896-905

Drusch, M., Del Bello, U., Carlier, S., Colin, O., Fernandez, V., Gascon, F., Hoersch, B., Isola, C., Laberinti, P., Martimort, P. 2012. Sentinel-2: ESA's optical high-resolution mission for GMES operational services. Remote Sensing of Environment, 120, 25-36

Duveiller, G., Hooker, J., Cescatti, A. 2018. The mark of vegetation change on Earth's surface energy balance. Nature Communications, 9, 1-12

Estoque, R.C., Ooba, M., Seposo, X.T., Togawa, T., Hijioka, Y., Takahashi, K., Nakamura, S. 2020. Heat health risk assessment in Philippine cities using remotely sensed data and social-ecological indicators. Nature Communications, 11, 1-12

Falasca, S., Ciancio, V., Salata, F., Golasi, I., Rosso, F., Curci, G. 2019. High albedo materials to counteract heat waves in cities: An assessment of meteorology, buildings energy needs and pedestrian thermal comfort. Building and Environment, 163, 106242

Falcone, J.A. 2016. US national categorical mapping of building heights by block group from Shuttle Radar Topography Mission data. http://dx.doi.org/10.5066/F7W09416

Feigenwinter, C., Vogt, R., Parlow, E., Lindberg, F., Marconcini, M., Del Frate, F., Chrysoulakis, N. 2018. Spatial distribution of sensible and latent

heat flux in the city of Basel (Switzerland). IEEE Journal of Selected Topics in Applied Earth Observations and Remote Sensing, 11, 2717-2723
Fortuniak, K., Pawlak, W., Siedlecki, M. 2013. Integral turbulence statistics over a central European city centre. Boundary-layer meteorology, 146, 257-276
Frantz, D., Schug, F., Okujeni, A., Navacchi, C., Wagner, W., van der Linden, S., Hostert, P. 2021. National-scale mapping of building height using Sentinel-1 and Sentinel-2 time series. Remote Sensing of Environment, 252, 11212
Ghimire, B., Williams, C.A., Masek, J., Gao, F., Wang, Z., Schaaf, C., He, T. 2014. Global albedo change and radiative cooling from anthropogenic land cover change, 1700 to 2005 based on MODIS, land use harmonization, radiative kernels, and reanalysis. Geophysical Research Letters, 41, 9087-9096
Gorelick, N., Hancher, M., Dixon, M., Ilyushchenko, S., Thau, D., Moore, R. 2017. Google Earth Engine: Planetary-scale geospatial analysis for everyone. Remote Sensing of Environment, 202, 18-27
Goret, M., Masson, V., Schoetter, R., Moine, M.-P. 2019. Inclusion of CO2 flux modelling in an urban canopy layer model and an evaluation over an old European city centre. Atmospheric Environment: X, 3, 100042
Groleau, D., Mestayer, P.G. 2013. Urban morphology influence on urban albedo: A revisit with the SOLENE model. Boundary-layer meteorology, 147, 301-327
Guo, T., He, T., Liang, S., Roujean, J.-L., Zhou, Y., Huang, X. 2022. Multi-decadal analysis of high-resolution albedo changes induced by urbanization over contrasted Chinese cities based on Landsat data. Remote Sensing of Environment, 269, 112832
Heris, M.P., Foks, N.L., Bagstad, K.J., Troy, A., Ancona, Z.H. 2020. A rasterized building footprint dataset for the United States. Scientific Data, 7, 1-10
He, T., Liang, S., Wang, D., Cao, Y., Gao, F., Yu, Y., Feng, M. 2018. Evaluating land surface albedo estimation from Landsat MSS, TM, ETM+, and OLI data based on the unified direct estimation approach. Remote Sensing of Environment, 204, 181-196
Hong, J., Lee, K., and Hong, J.-W.: Observational data of Ochang and Jungnang in Korea, 2020
Hsu, A., Sheriff, G., Chakraborty, T., Manya, D. 2021. Disproportionate exposure to urban heat island intensity across major US cities. Nature Communications, 12, 1-11
Hu, Y., Jia, G., Pohl, C., Zhang, X., van Genderen, J. 2016. Assessing surface albedo change and its induced radiation budget under rapid urbanization with Landsat and GLASS data. Theoretical and Applied Climatology, 123, 711-722
Huang, H., Xin, D., Hailin, Y., Xinhui, Z., Qi, J. 2020. Spatio-temporal mechanism underlying the effect of urban heat island on cardiovascular diseases. Iranian Journal of Public Health, 49, 1455
Hwang, Y., Ryu, Y., Qu, S. 2022. Expanding vegetated areas by human activities and strengthening vegetation growth concurrently explain the greening of Seoul. Landscape and Urban Planning, 227, 104518
Ishidoya, S., Sugawara, H., Terao, Y., Kaneyasu, N., Aoki, N., Tsuboi, K., Kondo, H. 2020. O 2: CO 2 exchange ratio for net turbulent flux observed in an urban area of Tokyo, Japan, and its application to an evaluation of anthropogenic CO 2 emissions. Atmospheric Chemistry and Physics, 20, 5293-5308
Järvi, L., Rannik, Ü., Kokkonen, T.V., Kurppa, M., Karppinen, A., Kouznetsov, R.D., Rantala, P., Vesala, T., Wood, C.R. 2018. Uncertainty of eddy covariance flux measurements over an urban area based on two towers. Atmospheric Measurement Techniques, 11, 5421-5438
Karsisto, P., Fortelius, C., Demuzere, M., Grimmond, C.S.B., Oleson, K., Kouznetsov, R., Masson, V., Järvi, L. 2016. Seasonal surface urban energy balance and wintertime stability simulated using three land-surface models in the high-latitude city H elsinki. Quarterly Journal of the Royal Meteorological Society, 142, 401-417
Kuang, W., Liu, A., Dou, Y., Li, G., Lu, D. 2019. Examining the impacts of urbanization on surface radiation using Landsat imagery. GIScience & Remote Sensing, 56, 462-484
Lang, N., Jetz, W., Schindler, K., Wegner, J.D. 2023. A high-resolution canopy height model of the Earth. Nature Ecology & Evolution, 7, 1778–1789
Lian, X., Jeong, S., Park, C.-E., Xu, H., Li, L.Z., Wang, T., Gentine, P., Peñuelas, J., Piao, S. 2022. Biophysical impacts of northern vegetation changes on seasonal warming patterns. Nature Communications, 13, 3925
Li, X., Gong, P., Zhou, Y., Wang, J., Bai, Y., Chen, B., Hu, T., Xiao, Y., Xu, B., Yang, J. 2020. Mapping global urban boundaries from the global artificial impervious area (GAIA) data. Environmental Research Letters, 15, 094044
Liang, S., Fang, H., Chen, M., Shuey, C.J., Walthall, C., Daughtry, C., Morisette, J., Schaaf, C., Strahler, A. 2002. Validating MODIS land surface reflectance and albedo products: Methods and preliminary results. Remote Sensing of Environment, 83, 149-162
Lin, X., Wu, S., Chen, B., Lin, Z., Yan, Z., Chen, X., Yin, G., You, D., Wen, J., Liu, Q. 2022. Estimating 10-m land surface albedo from Sentinel-2 satellite observations using a direct estimation approach with Google Earth Engine. ISPRS Journal of Photogrammetry and Remote Sensing, 194, 1-20
Lindberg, F., Holmer, B., Thorsson, S. 2008. SOLWEIG 1.0–Modelling spatial variations of 3D radiant fluxes and mean radiant temperature in complex urban settings. International Journal of Biometeorology, 52, 697-713
Lipson et al. (2022a) https://doi.org/10.5281/zenodo.7104984 (last accessed on November 6, 2022).
Lipson, M., Grimmond, S., Best, M., Chow, W., Christen, A., Chrysoulakis, N., Coutts, A., Crawford, B., Earl, S., Evans, J., Fortuniak, K., Heusinkveld, B. G., Hong, J.-W., Hong, J., Järvi, L., Jo, S., Kim, Y.-H., Kotthaus, S., Lee, K., Masson, V., McFadden, J. P., Michels, O., Pawlak, W., Roth, M., Sugawara, H., Tapper, N., Velasco, E., and Ward, H. C. (2022b): Harmonized gap-filled datasets from 20 urban flux tower sites, Earth System Science Data, 14, 5157-5178
Liu, X., Huang, Y., Xu, X., Li, X., Li, X., Ciais, P., Lin, P., Gong, K., Ziegler, A.D., Chen, A. 2020. High-spatiotemporal-resolution mapping of global urban change from 1985 to 2015. *Nature Sustainability*, 3, 564-570
Lucht, W., Schaaf, C.B., Strahler, A.H. 2000. An algorithm for the retrieval of albedo from space using semiempirical BRDF models. IEEE Transactions on Geoscience and Remote Sensing, 38, 977-998
Mann, H. 1945. Non-parametric tests against trend. Econometria. In: Chicago
Meng, L., Mao, J., Zhou, Y., Richardson, A.D., Lee, X., Thornton, P.E., Ricciuto, D.M., Li, X., Dai, Y., Shi, X. 2020. Urban warming advances spring phenology but reduces the response of phenology to temperature in the conterminous United States. Proceedings of the National Academy of Sciences, 117, 4228-4233
Menon, S., Akbari, H., Mahanama, S., Sednev, I., Levinson, R. 2010. Radiative forcing and temperature response to changes in urban albedos and associated CO2 offsets. Environmental Research Letters, 5, 014005
Morini, E., Touchaei, A.G., Castellani, B., Rossi, F., Cotana, F. 2016. The impact of albedo increase to mitigate the urban heat island in Terni (Italy) using the WRF model. *Sustainability*, 8, 999

Myhre, G., Shindell, D., Pongratz, J. 2014. Anthropogenic and natural radiative forcing
Oke, T.R. 1982. The energetic basis of the urban heat island. Quarterly Journal of the Royal Meteorological Society, 108, 1-24
Ouyang, Z., Sciusco, P., Jiao, T., Feron, S., Lei, C., Li, F., John, R., Fan, P., Li, X., Williams, C.A. 2022. Albedo changes caused by future urbanization contribute to global warming. Nature Communications, 13, 1-9
Piao, S., Wang, X., Park, T., Chen, C., Lian, X., He, Y., Bjerke, J.W., Chen, A., Ciais, P., Tømmervik, H. 2020. Characteristics, drivers and feedbacks of global greening. *Nature* Reviews Earth & Environment, 1, 14-27
Planet Team, Planet Imagery Product Specifications February 2021, Available online: https://www.planet.com/products/ (2022) (last accessed on November 6, 2022).
Qin, Y. 2015. Urban canyon albedo and its implication on the use of reflective cool pavements. Energy and Buildings, 96, 86-94
Qiu, S., Zhu, Z., Shang, R., Crawford, C.J. 2021. Can Landsat 7 preserve its science capability with a drifting orbit? Science of Remote Sensing, 4, 100026
Qu, Y., Liu, Q., Liang, S., Wang, L., Liu, N., Liu, S. 2013. Direct-estimation algorithm for mapping daily land-surface broadband albedo from MODIS data. IEEE Transactions on Geoscience and Remote Sensing, 52, 907-919
Rechid, D., Raddatz, T.J., Jacob, D. 2009. Parameterization of snow-free land surface albedo as a function of vegetation phenology based on MODIS data and applied in climate modelling. Theoretical and Applied Climatology, 95, 245-255
Ribeiro, H.V., Rybski, D., Kropp, J.P. 2019. Effects of changing population or density on urban carbon dioxide emissions. Nature Communications, 10, 1-9
Rosso, F., Golasi, I., Castaldo, V.L., Piselli, C., Pisello, A.L., Salata, F., Ferrero, M., Cotana, F., de Lieto Vollaro, A. 2018. On the impact of innovative materials on outdoor thermal comfort of pedestrians in historical urban canyons. Renewable Energy, 118, 825-839
Roth, M., Jansson, C., Velasco, E. 2017. Multi-year energy balance and carbon dioxide fluxes over a residential neighbourhood in a tropical city. International Journal of Climatology, 37, 2679-2698
Ryu, Y.-H., Bou-Zeid, E., Wang, Z.-H., & Smith, J.A. (2016). Realistic representation of trees in an urban canopy model. Boundary-layer meteorology, 159, 193-220
Santamouris, M., Fiorito, F. 2021. On the impact of modified urban albedo on ambient temperature and heat related mortality. Solar Energy, 216, 493-507
Schwaab, J., Meier, R., Mussetti, G., Seneviratne, S., Bürgi, C., Davin, E.L. 2021. The role of urban trees in reducing land surface temperatures in European cities. Nature Communications, 12, 1-11
Scott, C.P., Beckley, M., Phan, M., Zawacki, E., Crosby, C., Nandigam, V., Arrowsmith, R. 2022. Statewide USGS 3DEP Lidar Topographic Differencing Applied to Indiana, USA. Remote Sensing, 14, 847
Seto, K.C., Güneralp, B., Hutyra, L.R. 2012. Global forecasts of urban expansion to 2030 and direct impacts on biodiversity and carbon pools. Proceedings of the National Academy of Sciences, 109, 16083-16088
Shen, P., Zhao, S., Ma, Y. 2021. Perturbation of urbanization to Earth's surface energy balance. Journal of Geophysical Research: Atmospheres, 126, e2020JD033521
Shindell, D.T., Lamarque, J.-F., Schulz, M., Flanner, M., Jiao, C., Chin, M., Young, P., Lee, Y.H., Rotstayn, L., Mahowald, N. 2013. Radiative forcing in the ACCMIP historical and future climate simulations. Atmospheric Chemistry and Physics, 13, 2939-2974
Shuai, Y., Masek, J.G., Gao, F., Schaaf, C.B. 2011. An algorithm for the retrieval of 30-m snow-free albedo from Landsat surface reflectance and MODIS BRDF. Remote Sensing of Environment, 115, 2204-2216
Shuai, Y., Masek, J.G., Gao, F., Schaaf, C.B., He, T. 2014. An approach for the long-term 30-m land surface snow-free albedo retrieval from historic Landsat surface reflectance and MODIS-based a priori anisotropy knowledge. Remote Sensing of Environment, 152, 467-479
Stagakis, S., Chrysoulakis, N., Spyridakis, N., Feigenwinter, C., Vogt, R. 2019. Eddy Covariance measurements and source partitioning of CO2 emissions in an urban environment: Application for Heraklion, Greece. Atmospheric Environment, 201, 278-292
Stokes, G.M., Schwartz, S.E. 1994. The Atmospheric Radiation Measurement (ARM) Program: Programmatic background and design of the cloud and radiation test bed. Bulletin of the American Meteorological Society, 75, 1201-1222
Sulla-Menashe, D., Friedl, M.A. 2018. User guide to collection 6 MODIS land cover (MCD12Q1 and MCD12C1) product. USGS: Reston, VA, USA, 1, 18
Sun, L., Chen, J., Li, Q., Huang, D. 2020. Dramatic uneven urbanization of large cities throughout the world in recent decades. Nature Communications, 11, 1-9
Tang, R., Zhao, X., Zhou, T., Jiang, B., Wu, D., Tang, B. 2018. Assessing the impacts of urbanization on albedo in Jing-Jin-Ji Region of China. Remote Sensing, 10, 1096
Theil, H. 1950. A rank-invariant method of linear and polynomial regression analysis. Indagationes Mathematicae, 12, 173
Theobald, D.M., Kennedy, C., Chen, B., Oakleaf, J., Baruch-Mordo, S., Kiesecker, J. 2020. Earth transformed: detailed mapping of global human modification from 1990 to 2017. Earth System Science Data, 12, 1953-1972
Trlica, A., Hutyra, L., Schaaf, C., Erb, A., Wang, J. 2017. Albedo, land cover, and daytime surface temperature variation across an urbanized landscape. Earth's Future, 5, 1084-1101
Velasco, E., Perrusquia, R., Jiménez, E., Hernández, F., Camacho, P., Rodríguez, S., Retama, A., Molina, L. 2014. Sources and sinks of carbon dioxide in a neighborhood of Mexico City. Atmospheric Environment, 97, 226-238
UNDESA (United Nations Department of Economic and Social Affairs). 2019. World Population Prospects 2019: Highlights. Available at: https://population.un.org/wpp/Publications/Files/WPP2019_Highlights.pdf.
Wang, D., Liang, S., He, T., Yu, Y., Schaaf, C., Wang, Z. 2015. Estimating daily mean land surface albedo from MODIS data. Journal of Geophysical Research: Atmospheres, 120, 4825-4841
Wang, X., Xiao, J., Li, X., Cheng, G., Ma, M., Zhu, G., Altaf Arain, M., Andrew Black, T., Jassal, R.S. 2019. No trends in spring and autumn phenology during the global warming hiatus. Nature Communications, 10, 1-10
Wang, Z., Schaaf, C.B., Sun, Q., Shuai, Y., Román, M.O. 2018. Capturing rapid land surface dynamics with Collection V006 MODIS BRDF/NBAR/Albedo (MCD43) products. Remote Sensing of Environment, 207, 50-64
Ward, H., Evans, J.G., Grimmond, C.S.B. 2013. Multi-season eddy covariance observations of energy, water and carbon fluxes over a suburban area in Swindon, UK. Atmospheric Chemistry and Physics, 13, 4645-4666
Wong, N.H., Tan, C.L., Kolokotsa, D.D., Takebayashi, H. 2021. Greenery as a mitigation and adaptation strategy to urban heat. Nature Reviews Earth & Environment, 2, 166-181

Wu, S., Wen, J., Gastellu-Etchegorry, J.-P., Liu, Q., You, D., Xiao, Q., Hao, D., Lin, X., Yin, T. 2019. The definition of remotely sensed reflectance quantities suitable for rugged terrain. Remote Sensing of Environment, 225, 403-415

Wu, S., Wen, J., Xiao, Q., Liu, Q., Hao, D., Lin, X., You, D. 2018. Derivation of Kernel functions for Kernel-driven reflectance model over sloping terrain. IEEE Journal of Selected Topics in Applied Earth Observations and Remote Sensing, 12, 396-409

Wulder, M.A., Roy, D.P., Radeloff, V.C., Loveland, T.R., Anderson, M.C., Johnson, D.M., Healey, S., Zhu, Z., Scambos, T.A., Pahlevan, N. 2022. Fifty years of Landsat science and impacts. Remote Sensing of Environment, 280, 113195

Xu, X., AzariJafari, H., Gregory, J., Norford, L., Kirchain, R. 2020. An integrated model for quantifying the impacts of pavement albedo and urban morphology on building energy demand. Energy and Buildings, 211, 109759

Yang, C., Zhao, S. 2022. A building height dataset across China in 2017 estimated by the spatially-informed approach. Scientific Data, 9, 1-11

Yang, X., Li, Y. 2015. The impact of building density and building height heterogeneity on average urban albedo and street surface temperature. Building and environment, 90, 146-156

Zanaga, D., Van De Kerchove, R., De Keersmaecker, W., Souverijns, N., Brockmann, C., Quast, R., Wevers, J., Grosu, A., Paccini, A., Vergnaud, S. 2021. ESA WorldCover 10 m 2020 v100

Zhang, H., Roy, D.P. 2016. Landsat 5 Thematic Mapper reflectance and NDVI 27-year time series inconsistencies due to satellite orbit change. Remote Sensing of Environment, 186, 217-2

Zhang, Q., Seto, K.C. 2011. Mapping urbanization dynamics at regional and global scales using multi-temporal DMSP/OLS nighttime light data. *Remote Sensing of Environment*, 115, 2320-2329

Zhang, W., Randall, M., Jensen, M.B., Brandt, M., Wang, Q., Fensholt, R. 2021. Socio-economic and climatic changes lead to contrasting global urban vegetation trends. Global Environmental Change, 71, 102385

Zhou, Y., Li, X., Chen, W., Meng, L., Wu, Q., Gong, P., Seto, K.C. 2022. Satellite mapping of urban built-up heights reveals extreme infrastructure gaps and inequalities in the Global South. Proceedings of the National Academy of Sciences, 119, e2214813119

Table 1. *Datasets used in this study by type.*

Usage type	Dataset	Spatial extent	Resolution (m)	Frequency	Period	Purpose description	Reference
Surface reflectance	Landsat-5 SR	Global cities	30	16-day	1986-2011	Surface albedo & vegetation cover	Gorelick et al. 2017
	Landsat-7 SR	Global cities	30	16-day	2012-2013	Surface albedo & vegetation cover	Gorelick et al. 2017
	Landsat-8 SR	Global cities	30	16-day	2014-2020	Surface albedo & vegetation cover	Gorelick et al. 2017
Surface BRDF	MCD43A1	Global	500	Daily	2000-2020	BRDF database for LUT training	Gorelick et al. 2017; Wang et al. 2018
Surface albedo	Tower-based measurements	Table 2	-	10-30 min	Table 2	Albedo evaluation	Lipson et al. 2022a,b
	MCD43A3	Global	500	Daily	2000-2020	Albedo spatiotemporal analysis	Wang et al. 2018
Land cover type	ESA WorldCover	Global	10	Annual	2020	BRDF training sample selection	Zanaga et al. 2021
	MCD12Q1	Global	500	Annual	2001-2020	BRDF training sample selection	Gorelick et al. 2017; Wang et al. 2018
Solar radiation	BaRAD	Global	0.5° x 0.625°	Monthly	1980-2019	1) Diffuse skylight ratio estimate 2) Surface radiative forcing estimate	Chakraborty and Lee, 2021

Table 2. *Flux sites used for albedo evaluation, Tower height and impervious area fraction are available from Lipson et al.(2022a) and https://mcr.unibas.ch/dev/sqldb/index.php?nav=dbplot. Footprint diameter (D) of tower measurement (D = 2H • tan (FOV/2)) is calculated from tower height (H) and sensor's field of view (FOV) according to Román et al. 2009.*

Site name	City	Country	Latitude (°)	Longitude (°)	Tower height (m)	Footprint diameter (m)	Impervious area fraction	Observation years	Reference
Amsterdam	Amsterdam	Netherlands	52.367	4.893	40	505	0.68	2019-2020	-
Baltimore	Baltimore	United States	39.413	-76.522	37	467	0.31	2002-2006	Crawford et al. 2011
Capitole	Toulouse	France	43.604	1.445	48	606	0.90	2004-2005	Goret et al. 2019
Escandon	Mexico	Mexico	19.404	-99.176	37	467	0.94	2011-2012	Velasco et al. 2014
Heckor	Heraklion	Greece	35.336	25.133	27	341	0.92	2019-2020	Stagakis et al. 2019
Jungnang	Seoul	South Korea	37.591	127.079	42	524	0.97	2017-2019	Hong et al. 2020
KingsCollege	London	UK	51.512	-0.117	50	631	0.79	2012-2013	Bjorkegren et al. 2015
Klingelbergstrasse	Basel	Switzerland	47.562	7.581	40	505	0.79	2003-2021	Feigenwinter et al. 2018
KlingelbstrStr.schlucht	Basel	Switzerland	47.561	7.581	2	25	0.79	2014-2020	Feigenwinter et al. 2018
Kumpula	Helsinki	Finland	60.203	24.961	31	391	0.46	2011-2021	Karsisto et al. 2016
Lipowa	Łódź	Poland	51.763	19.445	37	467	0.76	2008-2012	Fortuniak et al. 2013
Narutowicza	Łódź	Poland	51.773	19.481	42	530	0.65	2008-2012	Fortuniak et al. 2013
Ochang	Ochang	South Korea	36.720	127.434	19	240	0.47	2015-2017	Hong et al. 2020
Preston	Melbourne	Australia	-37.731	145.015	40	505	0.62	2003-2004	Coutts et al. 2007
Sunset	Vancouver	Canada	49.226	-123.078	24	303	0.68	2012-2016	Crawford and Christen, 2015
SurreyHills	Melbourne	Australia	-37.827	145.099	38	480	0.54	2004-2004	Coutts et al. 2007
Swindon	Swindon	UK	51.585	-1.798	13	158	0.49	2011-2013	Ward et al. 2013
TelokKurau	Singapore	Singapore	1.314	103.911	21	253	0.85	2006-2007	Roth et al. 2017
Torni	Helsinki	Finland	60.168	24.939	60	758	0.77	2011-2013	Järvi et al. 2018
WestPhoenix	Arizona	United States	33.484	-112.143	22	278	0.48	2011-2012	Chow, 2017

Yoyogi	Tokyo	Japan	35.665	139.685	52	657	0.92	2016-2020	Ishidoya et al. 2020

Note: The KlingelbstrStr.schlucht site with a 2-m tower height observes the fluxes of grassland in urban environment.

Supplementary Materials

Table S1. *Spectral configurations of Landsat-5 TM, Landsat-7 ETM+, and Landsat-8 OLI sensors. NIR: near-infrared; SWIR: shortwave-infrared. The spectral information is available from the United States Geological Survey (USGS): https://www.usgs.gov/faqs/what-are-band-designations-landsat-satellites*

Band name	*Sensor and wavelength (μm)*		
	Landsat-5 TM	*Landsat-7 ETM+*	*Landsat-8 OLI*
Coastal blue	—	—	*0.43-0.45*
Blue	*0.45-0.52*	*0.45-0.52*	*0.45-0.51*
Green	*0.52-0.60*	*0.52-0.60*	*0.53-0.59*
Red	*0.63-0.69*	*0.63-0.69*	*0.64-0.67*
NIR	*0.76-0.90*	*0.77-0.90*	*0.85-0.88*
SWIR1	*1.55-1.75*	*1.55-1.75*	*1.57-1.65*
SWIR2	*2.08-2.35*	*2.09-2.35*	*2.11-2.29*

Table S2. *Building footprint stock datasets used for analyzing the potential influence of 3D urban building landscape on the spatiotemporal trends of surface albedo.*

Dataset name	*Spatial extent*	*Resolution (m)*	*Period*	*Reference*
Rasterized building footprint	*United States*	*30*	*2018*	*Heris et al. 2020*
Building height	*Germany*	*10*	*2018*	*Frantz et al. 2021*
Building height	*United States*	*30*	*2000*	*Falcone, 2016*
Building height	*China*	*1000*	*2017*	*Yang and Zhao, 2022*

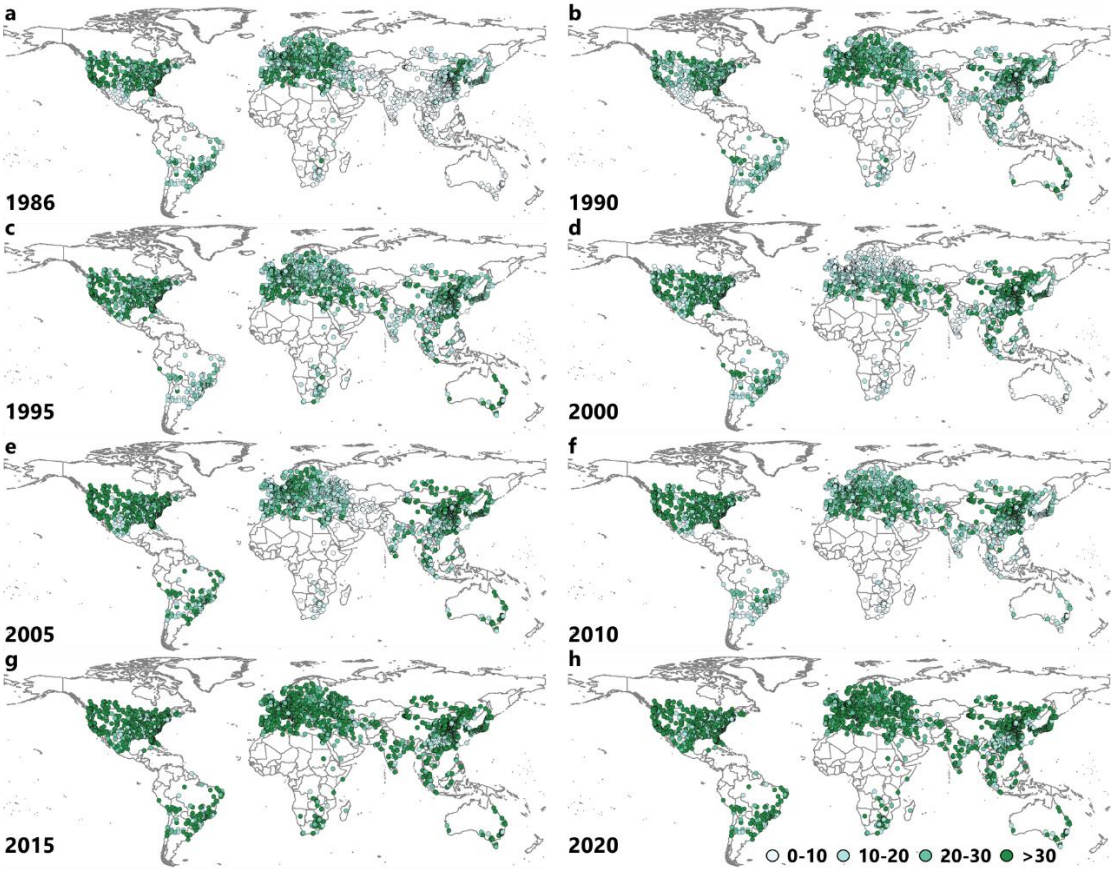

Fig. S1. *Spatial patterns of annual numbers of available Landsat images for 3037 global cities for* ***(a)*** *1986,* ***(b)*** *1990,* ***(c)*** *1995,* ***(d)*** *2000,* ***(e)*** *2005,* ***(f)*** *2010,* ***(g)*** *2015, and* ***(h)*** *2020.*

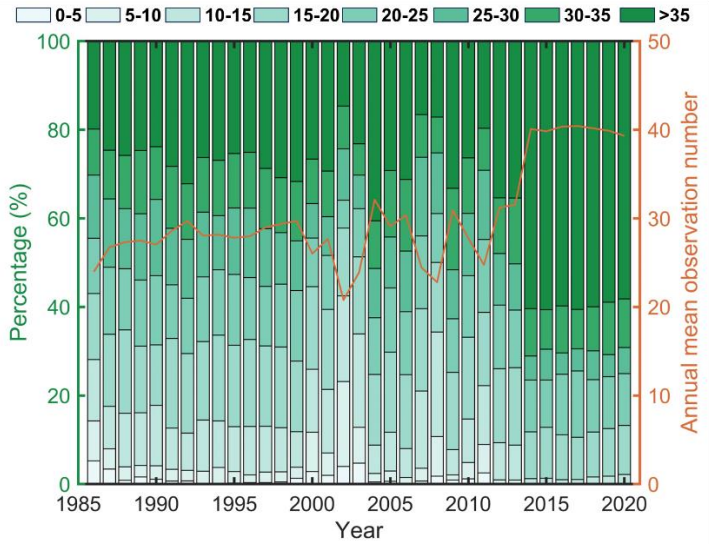

Fig. S2. *Annual number of available Landsat images for 3037 global cities over 35 years (1986-2020). Left axis: the percentage of cities with different levels of available Landsat image numbers from 0-35 with an interval of 5 within a one-year cycle. Right axis: the mean annual Landsat image number for these cities.*

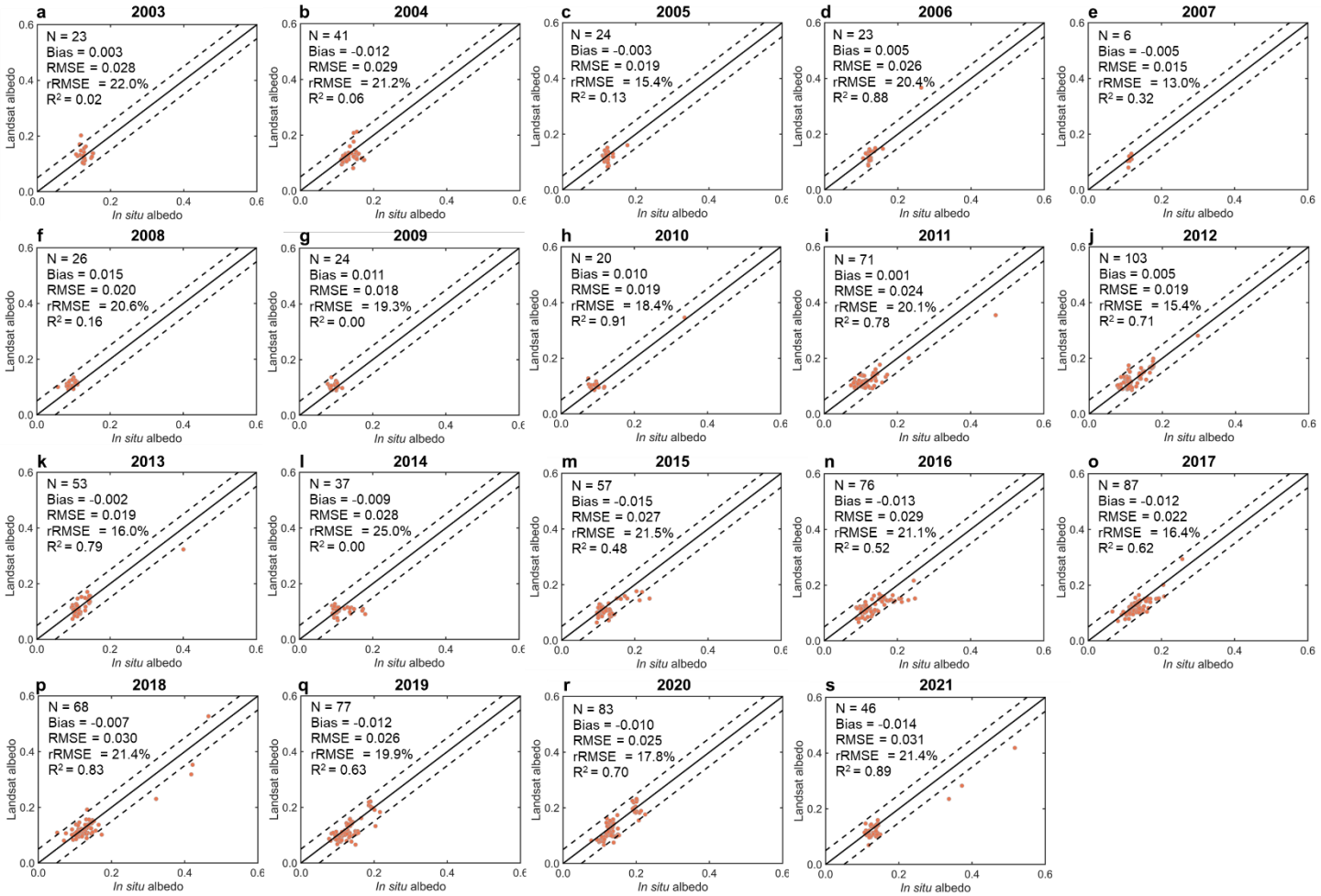

Fig. S3. *Annual evaluation of Landsat-derived albedo with flux-tower measurements from 2003 to 2021. The following comparison statistics are calculated: N (number of Landsat data observed on the same date as flux-tower measurements), bias (mean difference between Landsat-derived and tower-based albedo), RMSE (root-mean-square-error), rRMSE (relative RMSE, ratio between RMSE and measured albedo mean) and R^2 (coefficient of determination), 1:1 line (solid line), error lines of -0.05 and 0.05 (dashed line).*

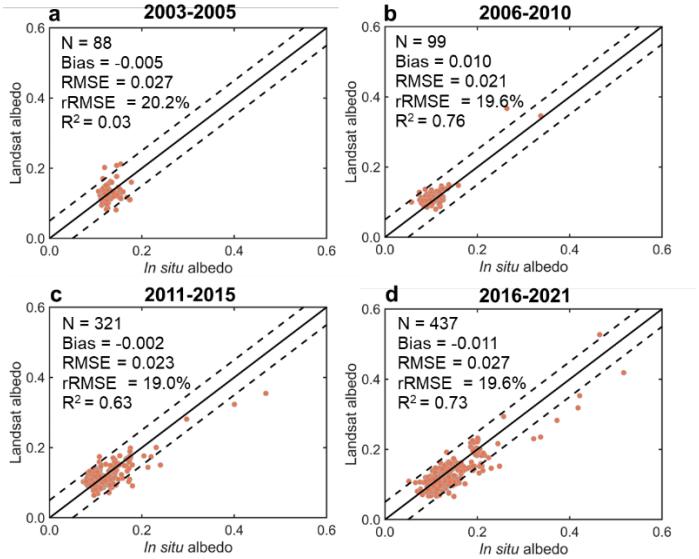

Fig. S4. *Evaluation of Landsat-derived albedo with flux-tower measurements from 2003 to 2021 for* ***(a)*** *2003-2005,* ***(b)*** *2006-2010,* ***(c)*** *2011-2015, and* ***(d)*** *2016-2021. The following comparison statistics are calculated: N (number of Landsat data observed on the same date as flux-tower measurements), bias (mean difference between Landsat-derived and tower-based albedo), RMSE (root-mean-square-error), rRMSE (relative RMSE, ratio between RMSE and measured albedo mean) and R^2 (coefficient of determination), 1:1 line (solid line), error lines of -0.05 and 0.05 (dashed line).*

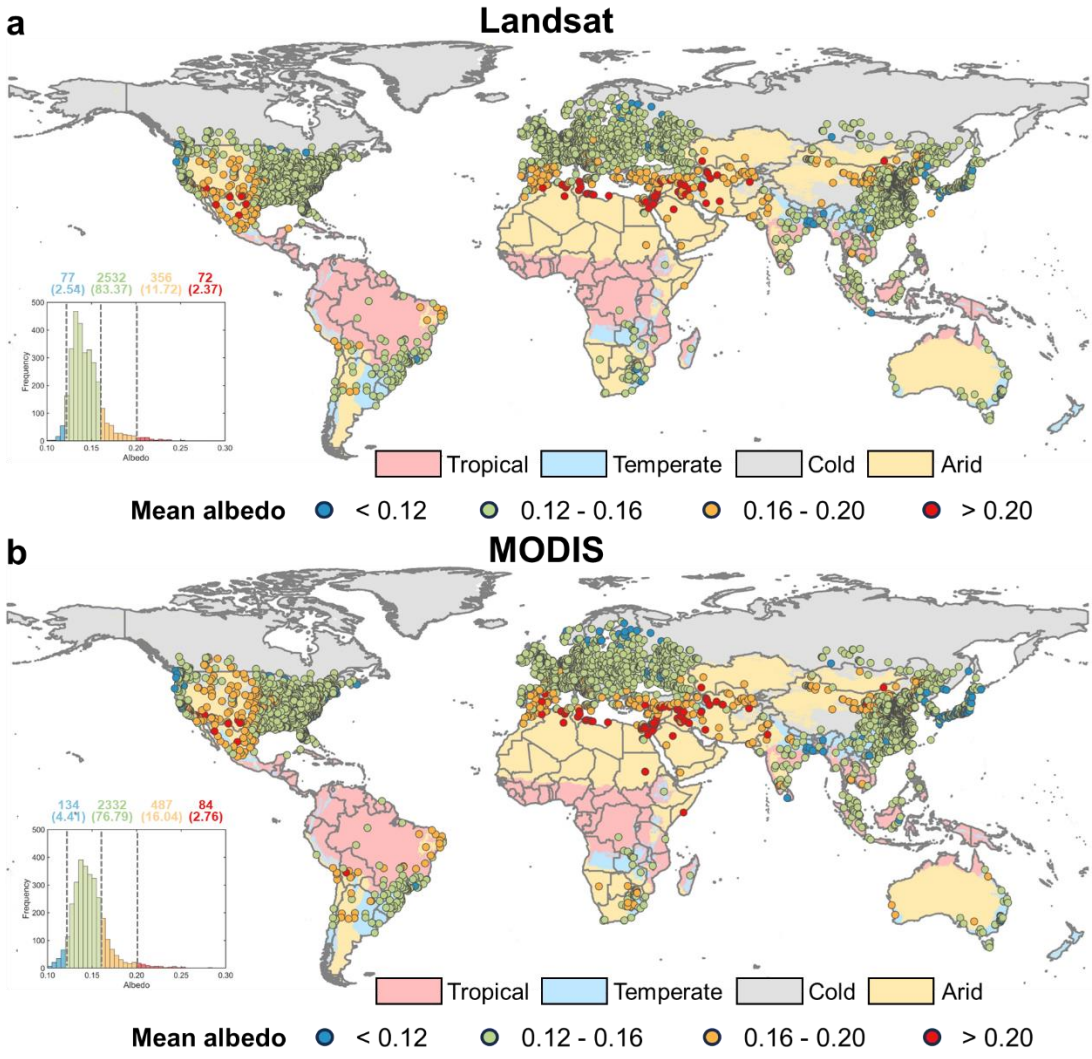

Fig. S5*. City-level average annual albedo (lower key) derived from 20-year (2001-2020)* ***(a)*** *Landsat and* ***(b)*** *MODIS data for 3037 global cities mapped onto 1-km Köppen-Geiger climate (Beck et al. 2018) (upper key), with the number of cities (and the associated percentage in parentheses) given above the inserted histogram.*

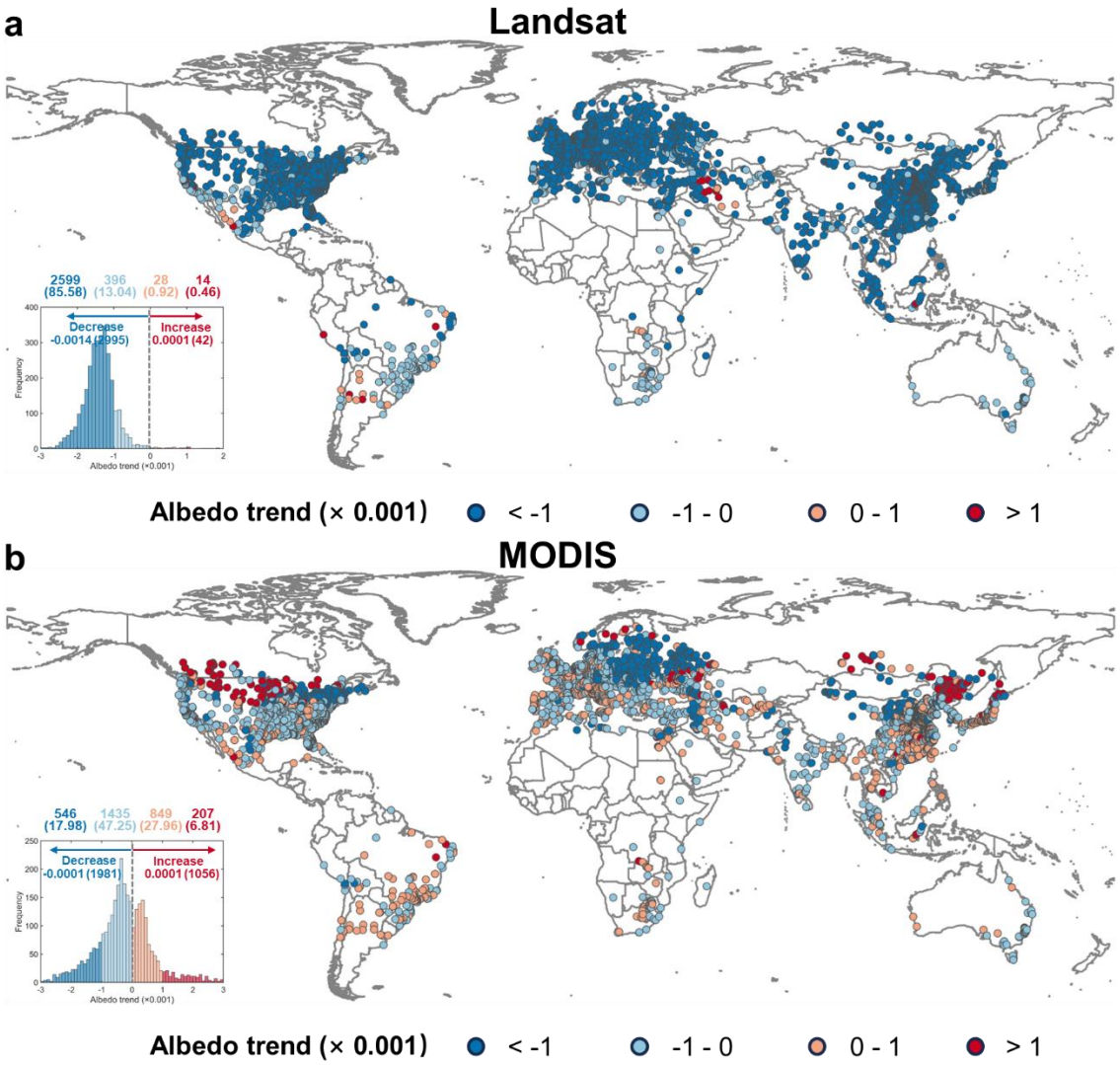

Fig. S6. *Spatial patterns of* ***(a)*** *Landsat- and* ***(b)*** *MODIS-derived city-level albedo trend for 3037 global cities over 35 years (1986-2020), with the histogram (albedo key) of the albedo trend and the number of cities (with the associated percentage in parentheses) given above the inserted histogram.*

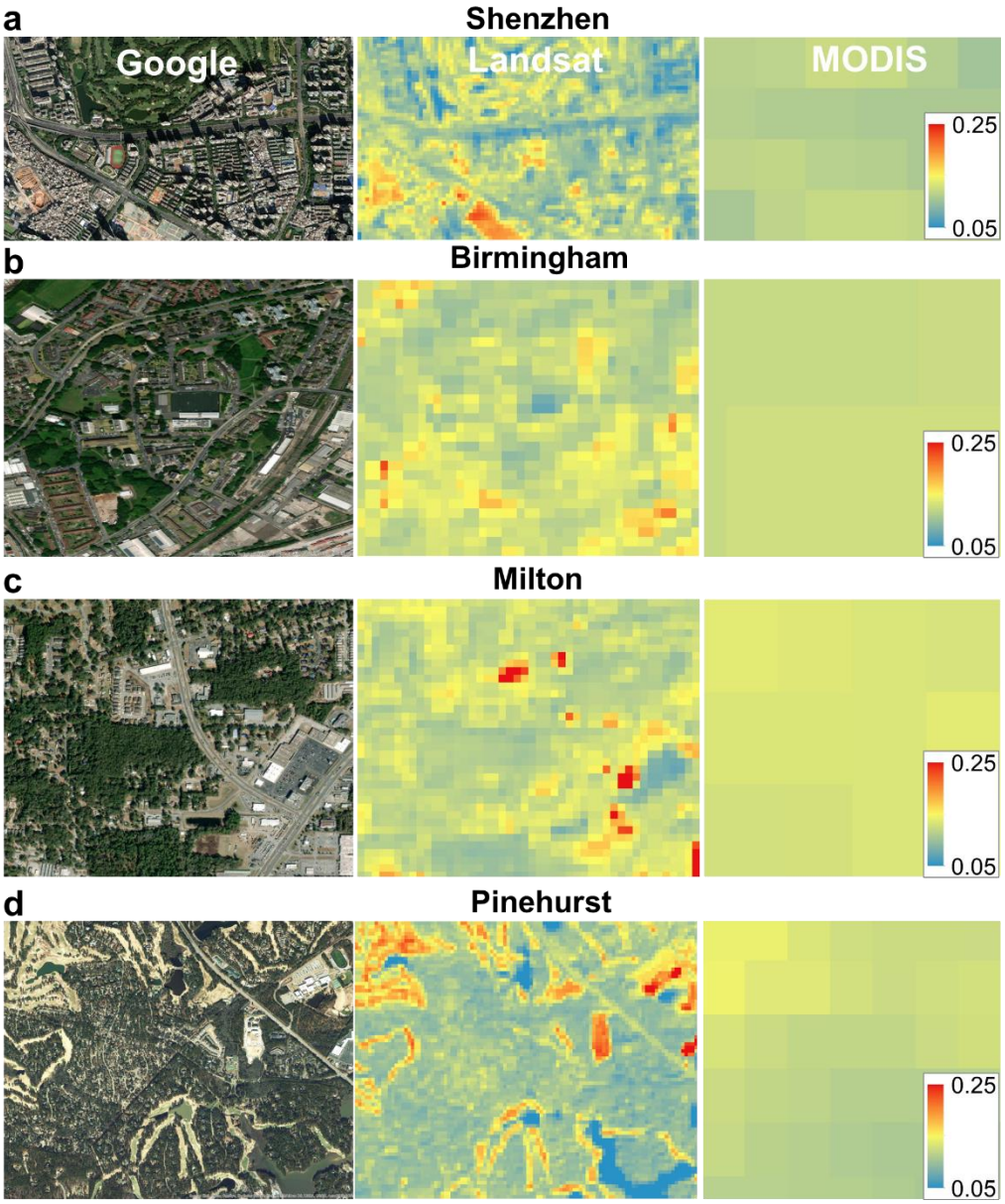

Fig. S7*. Comparisons between Landsat and MODIS in capturing heterogeneous albedo of urban area over* ***(a)*** *Shenzhen, China,* ***(b)*** *Birmingham, , United Kingdom,* ***(c)*** *Milton, Florida, United States, and* ***(d)*** *Pinehurst, North Carolina, United States. First column: Google Basemap image. Middle column: Landsat-derived albedo. Third column: MODIS albedo.*

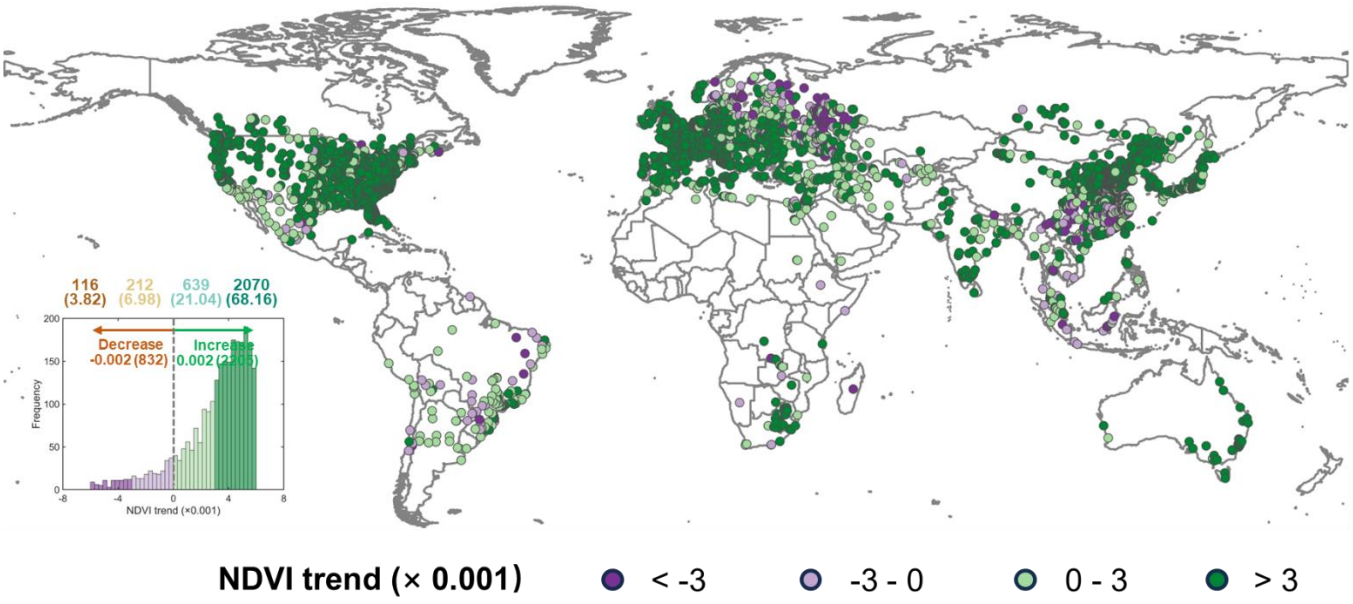

Fig. S8. *Spatial patterns of Landsat-derived city-level normalized difference vegetation index (NDVI) trend for 3037 global cities over 20 years (2001-2020), with the histogram (NDVI key) of the NDVI trend and the number of cities (with the associated percentage in parentheses) given above the inserted histogram.*

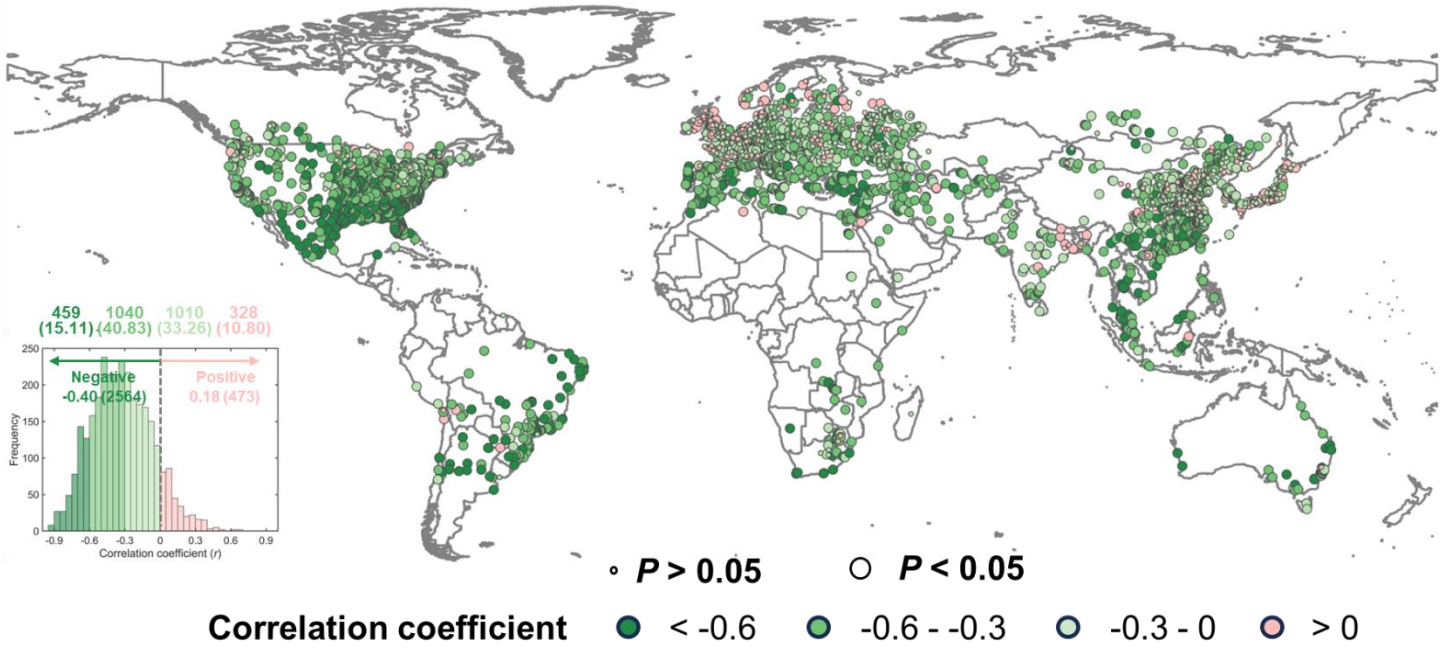

Fig. S9. *Spatial patterns of the intra-city correlation between urban normalized difference vegetation index (NDVI) and albedo trend for 3037 global cities over 20 years (2001-2020), with the histogram (correlation coefficient key) of the city-level albedo trend and the number of cities (with the associated percentage in parentheses) given above the inserted histogram. Large bubble sizes represent a statistically significant level of 0.05 (p-value <0.05) and small bubble sizes represent a non-significant trend with p-value >0.05.*

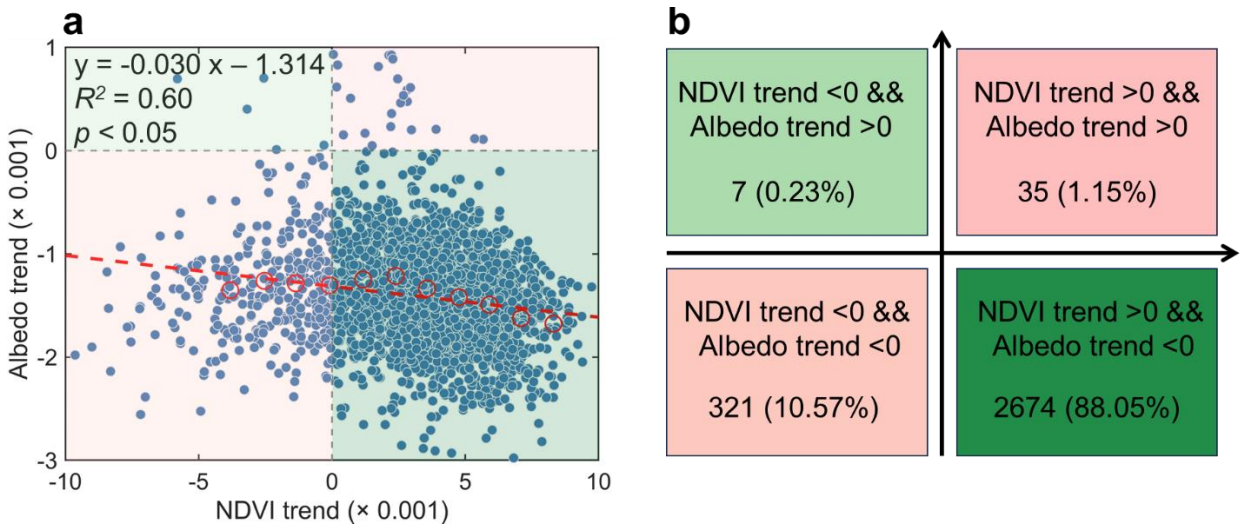

Fig. S10. *Associations between city-level normalized difference vegetation index (NDVI) and surface albedo trends for 3037 global cities over 35 years (1986-2020), with* ***(a)*** *scatter plot and* ***(b)*** *statistics of NDVI and albedo trend consistency. In* ***(a)****, the city-level trends are averaged from pixel-level trends that are statistically significant at a level of 0.05, using the non-parametric Mann-Kendall and Theil–Sen slope estimator approaches. A zonal analysis is used to refine the association results by averaging the NDVI and albedo trend pairs (red circles) within each 10% NDVI interval for the linear regression (red dashed line).*

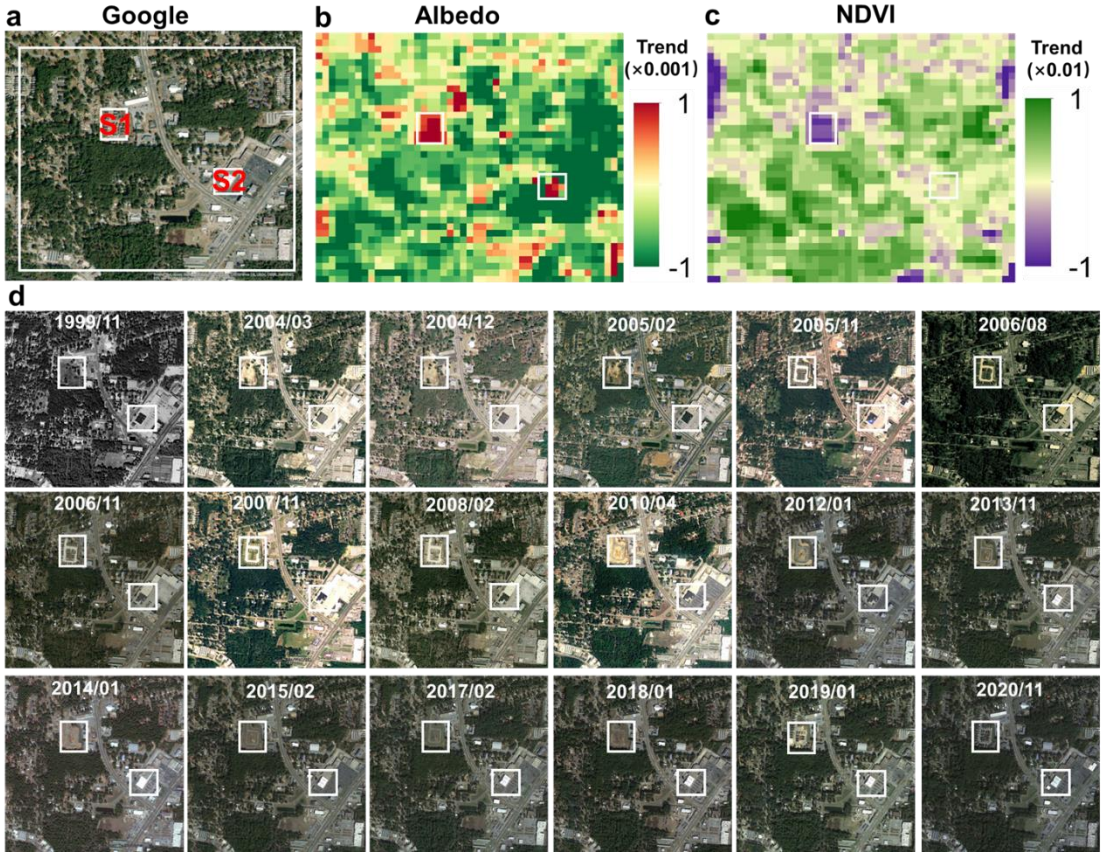

Fig. S11. *Examples showing the close association between surface albedo change and urbanization in Milton city, Florida, United States, based on the maps of* ***(a)*** *Google Earth satellite image,* ***(b)*** *albedo trend,* ***(c)*** *NDVI trend, and* ***(d)*** *Google Earth historic images from 2000 to 2020 with specific observation areas highlighted with white boxes. Two sites, S1 and S2 marked red in* ***(a)****, are shown enlarged in* ***Fig. S12*** *to demonstrate the controls of building construction and rooftop renewal can have on surface albedo change.*

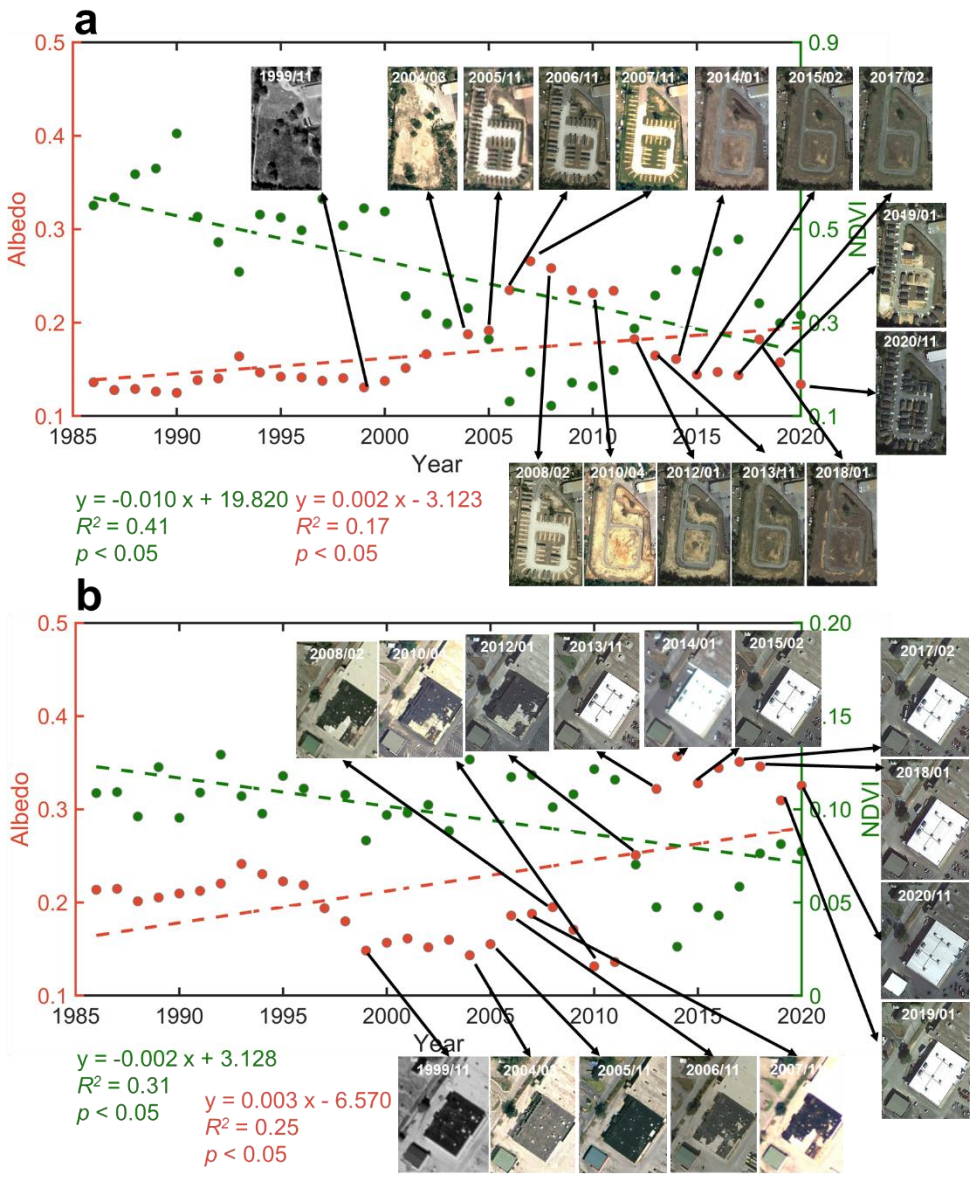

Fig. S12. *Influence of* ***(a)*** *building construction (****S1*** *in* ***Fig. S11a****) and* ***(b)*** *rooftop renewal (****S2*** *in* ***Fig. S11a****) on surface albedo in two urban fringe areas in Milton city, Florida, United States. High-resolution Google Earth satellite images are inserted to demonstrate the changes over time.*

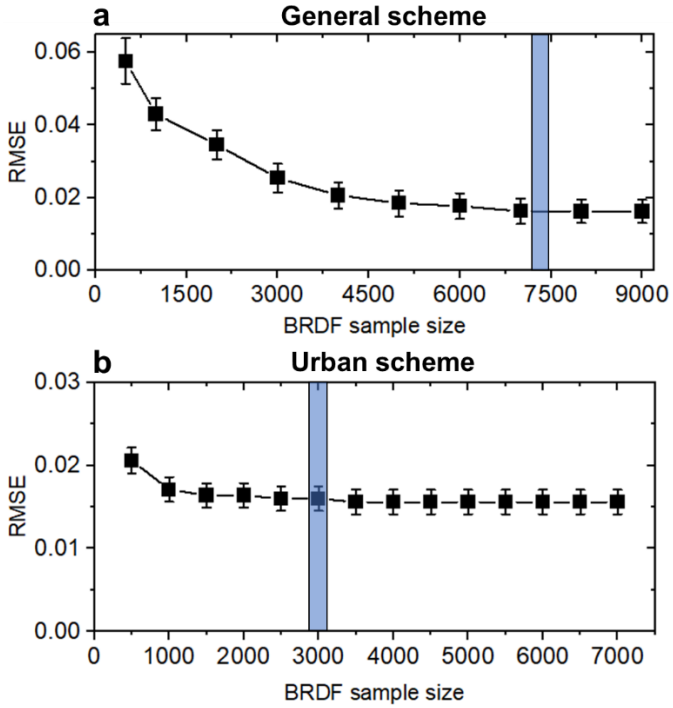

Fig. S13. *Sensitivity analysis showing the impacts of BRDF sample size on the theoretical accuracy and uncertainty of the proposed direct estimation approach with training and testing BRDF datasets from* ***(a)*** *16 IGBP land cover types (****general scheme used in the main text****),* ***(b)*** *pure urban land cover (****urban scheme****). The root-mean-square-error (RMSE) is derived from the surface albedo retrieved with the Look-Up-Table (LUT)-based approach, and the simulated broadband albedo is calculated using the testing components of MODIS BRDF data. The central mark and error bar of boxplot refer to the mean and standard deviation of the fitted RMSE, respectively. The light blue bars show the optimized BRDF sample sizes.*

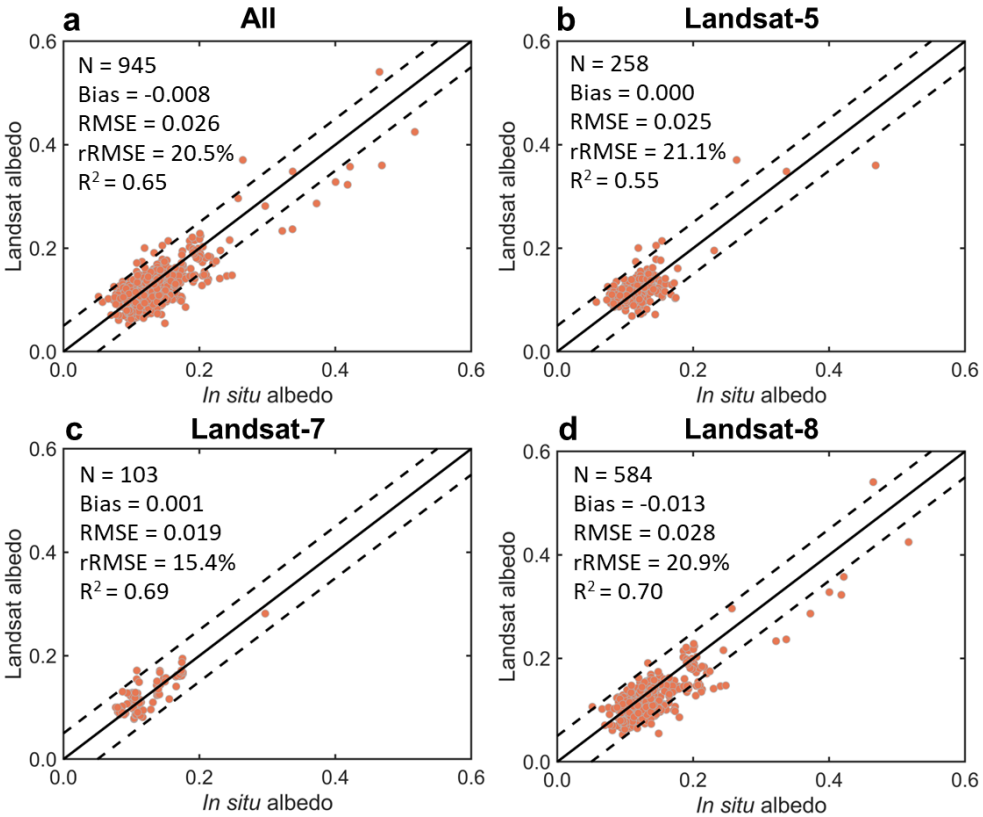

Fig. S14. *Evaluation of Landsat-derived albedo with flux-tower measurements using* ***urban scheme*** *training samples for* ***(a)*** *all three Landsat satellites,* ***(b)*** *Landsat-5,* ***(c)*** *Landsat-7, and* ***(d)*** *Landsat-8. The following comparison statistics are calculated: N (number of Landsat data observed on the same date as flux-tower measurements), bias (mean difference between Landsat-derived and tower-based albedo), RMSE (root-mean-square-error), rRMSE (relative RMSE, ratio between RMSE and measured albedo mean) and R^2 (coefficient of determination), 1:1 line (solid line), error lines of -0.05 and 0.05 (dashed line).*

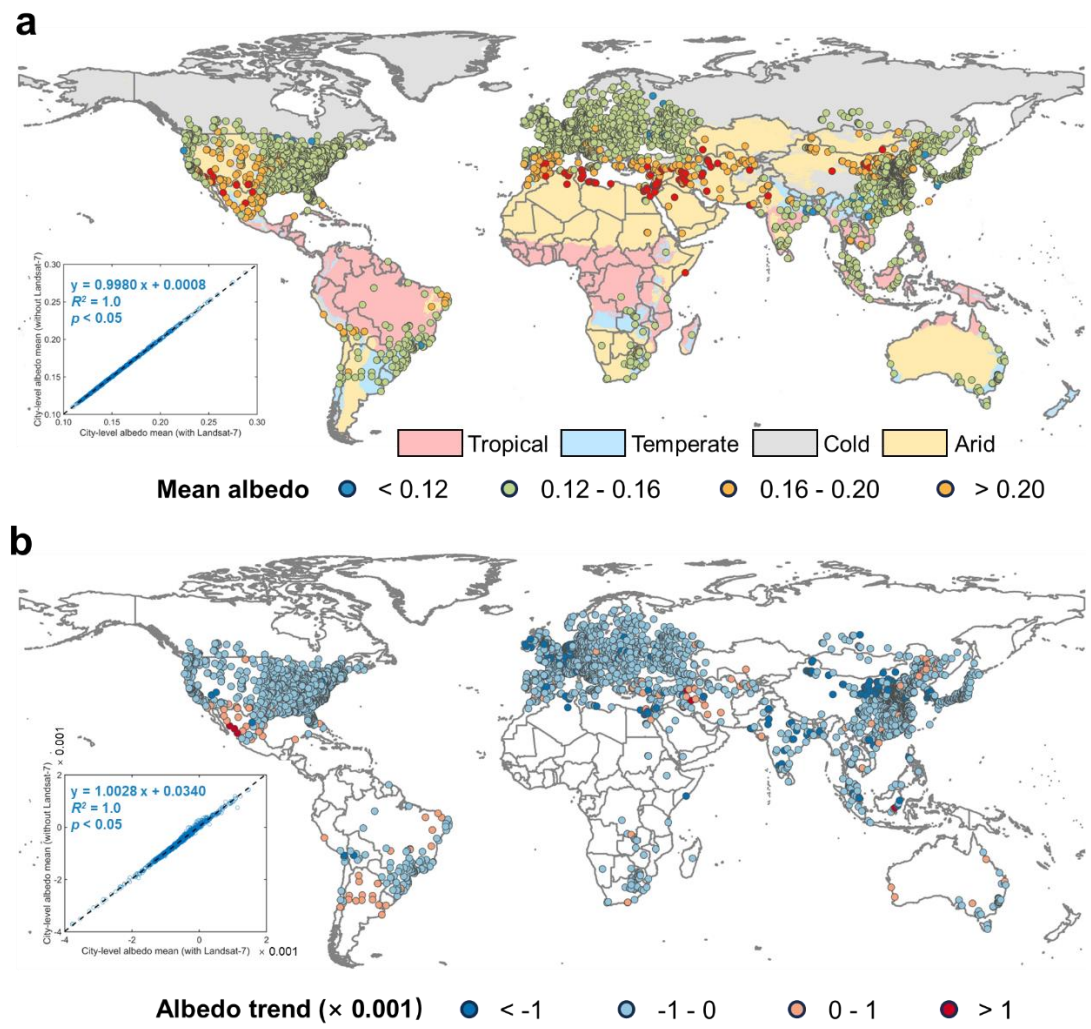

Fig. S15. *Sensitivity analysis regarding the impacts of scan line corrector (SLC) failure in Landsat-7 on the annual mean* ***(a)*** *and* ***(b)*** *long-term trend of urban albedo using time series without Landsat-7 observations. Inserted scatter plots are the associations between the albedo results with (****Figs. 5*** *and* ***6****) and without (****Fig. S15a*** *and* ***b****) Landsat-7 data.*

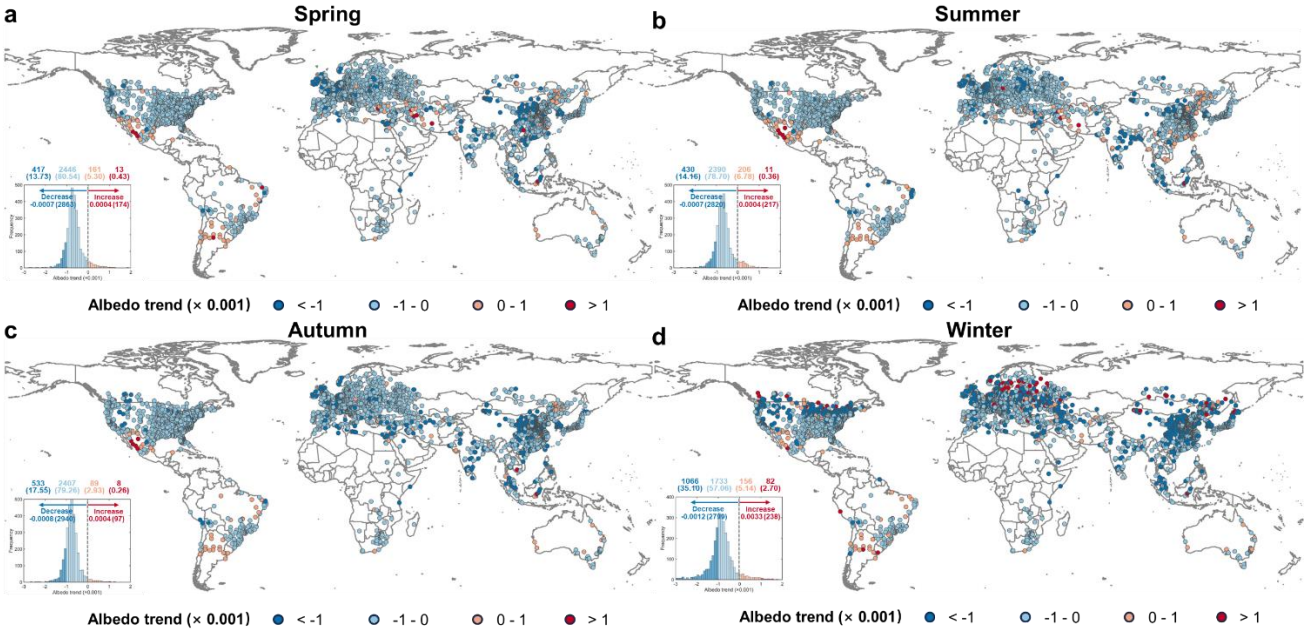

Fig. S16. *Spatial patterns of the Landsat-derived albedo trend for 3037 global cities over 35 years (1986-2020) for* ***(a)*** *spring,* ***(b)*** *summer,* ***(c)*** *autumn, and* ***(d)*** *winter seasons, with the histogram (albedo key) of the city-level albedo trend and the number of cities (with the associated percentage in parentheses) given above the inserted histogram.*

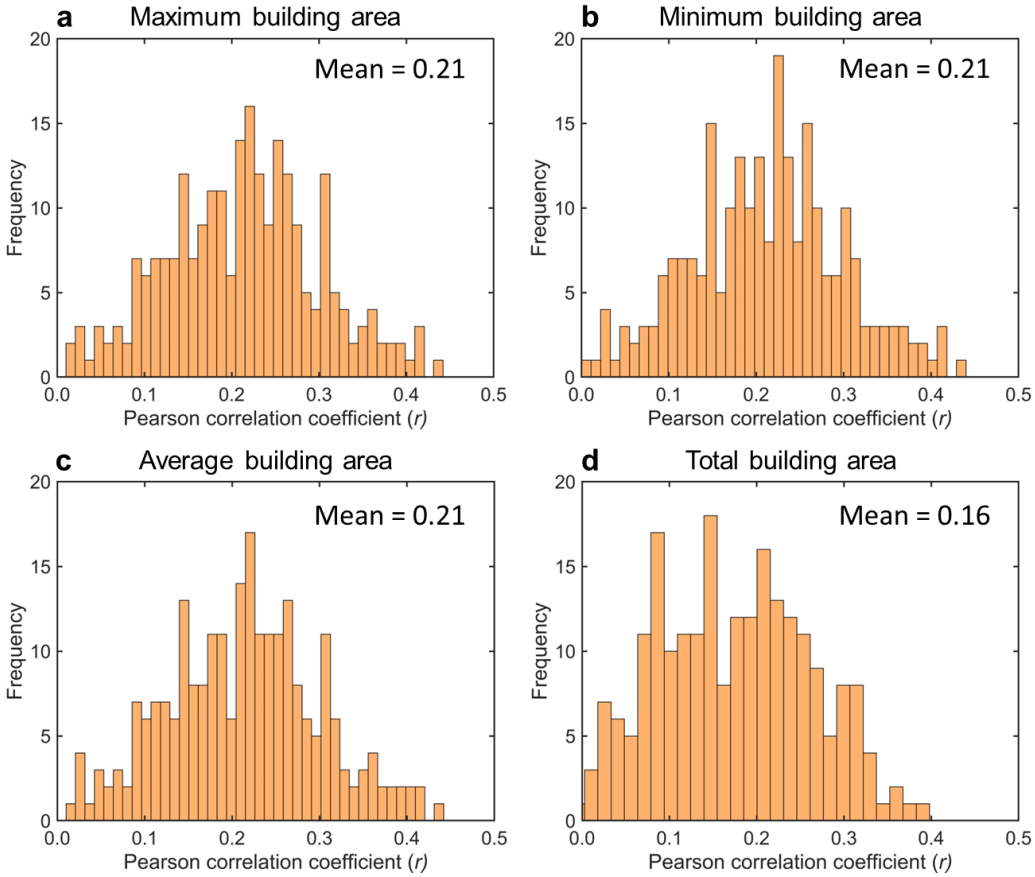

Fig. S17*. Correlation between surface albedo and 30-m-resolution building area for 242 cities in the United States (Heris et al. 2020), for* ***(a)*** *maximum building area,* ***(b)*** *minimum building area,* ***(c)*** *average building area, and* ***(d)*** *total building area within 30-m raster pixels.*

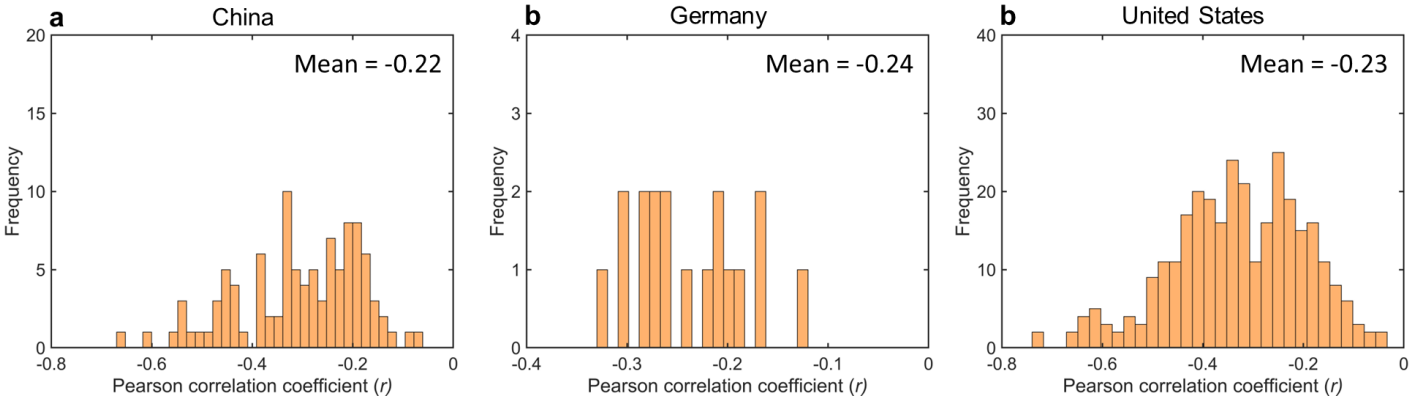

Fig. S18. *Correlation between surface albedo and three building height products for urban areas in* ***(a)*** *China using 1-km-resolution building height data of 120 cities (Yang and Zhao et al. 2022), where Landsat data is resampled from 30-m to 1-km resolution for comparison,* ***(b)*** *Germany using 10-m-resolution building height data of 18 cities (Frantz et al. 2021), which is resampled to 30-m resolution for comparison, and* ***(c)*** *United States using 30-m-resolution building height data of 372 cities (Falcone, 2016).*

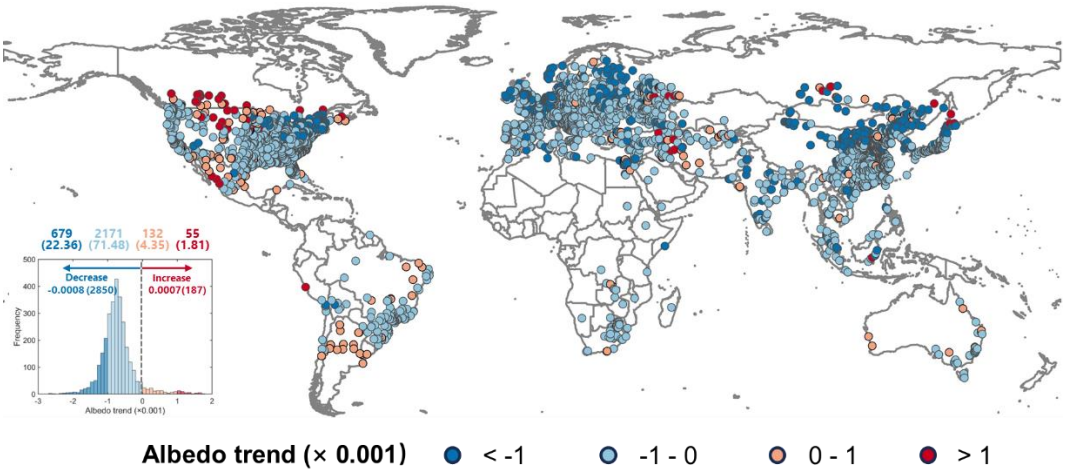

Fig. S19. *Spatial patterns of the Landsat-derived albedo trend with snow effect for 3037 global cities over 35 years (1986-2020), with the histogram (albedo key) of the city-level albedo trend and the number of cities (with the associated percentage in parentheses) given above the inserted histogram.*

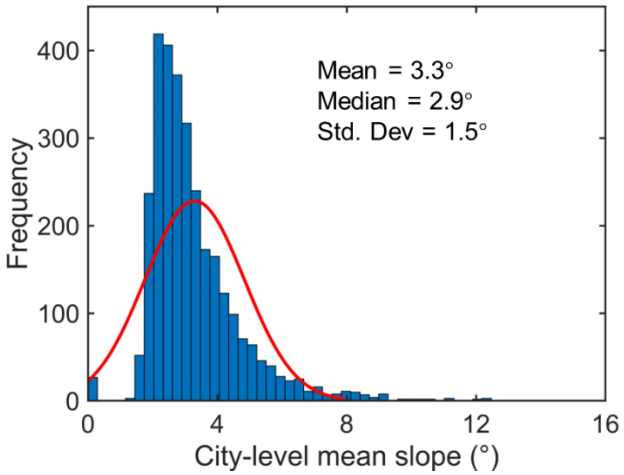

Fig. S20*. Histogram of city-level mean slope for 3037 global cities extracted from the 30-m-resolution ASTER Global Digital Elevation Model (ASTER GDEM, Gorelick et al. 2017) dataset. The distribution of city-level mean slope is fitted by a normal density function, where the mean, median, and stand deviation of slope is shown on the figure.*